Volume 12
Number 3

December *2010*
(ISSN 1109-1606)

Journal of APPLIED ELECTROMAGNETISM

JAE

Trans Black Sea Region Union of Applied Electromagnetism
BSUAE

Institute of Communication and Computer Systems

Athens - GREECE

Volume 12 December 2010
Number 3 (ISSN 1109-1606)

JOURNAL
OF
APPLIED ELECTROMAGNETISM

Trans Black Sea Region Union of Applied Electromagnetism

BSUAE

Institute of Communication and Computer Systems

Athens - GREECE

Volume 12 **Number 3**

December 2010

TRANS BLACK SEA REGION UNION OF APPLIED ELECTROMAGNETISM (BSUAE)

JOURNAL OF APPLIED ELECTROMAGNETISM

Institute of Communication and Computer Systems
Athens - GREECE

Editor: Panayiotis Frangos (Greece), pfrangos@central.ntua.gr

Honorary Editor: Nikolaos K. Uzunoglu (Greece), nuzu@central.ntua.gr

Board of Associate Editors

D. Dimitrov (Bulgaria), dcd@tu-sofia.bg
V. Dumbrava (Lithuania), vydum@ktu.lt
G. Georgiev (Bulgaria), gngeorgiev@yahoo.com
G. Matsopoulos (Greece), gmatso@esd.ece.ntua.gr

Editorial Board

ALBANIA
G. Bardhyf, bardhylgolemi@live.com
C. Pirro, p_cipo@yahoo.com

ARMENIA
H. Bagdasarian, hovik@seua.sci.am
H. Terzian, hterzian@seua.sci.am

BULGARIA
A. Antonov, asantonov@abv.bg
A. Lazarov, lazarov@bfu.bg
S. Savov, savovsv@yahoo.com

GEORGIA
R. Zaridze, rzaridze@laetsu.org

GERMANY
M. Georgieva – Grosse, mariana.georgieva-grosse@de.bosch.com

GREECE
H. Anastassiu, ANASTASIOU.Christos@haicorp.com
I. Avramopoulos, hav@mail.ntua.gr
G. Fikioris, gfiki@cc.ece.ntua.gr
J. Kanellopoulos, ikanell@cc.ece.ntua.gr
G. Karagiannidis, geokarag@auth.gr
G. Kliros, gsksma@hol.gr
T. Mathiopoulos, mathio@space.noa.gr
C. Moschovitis, harism@noc.ntua.gr
K. Nikita, knikita@cc.ece.ntua.gr
I. Ouranos, iouranos@central.ntua.gr
E. Papkelis, spapkel@central.ntua.gr
J. Sahalos, sahalos@auth.gr
M. Theologou, theolog@cs.ntua.gr

JORDAN
N. Dib, nihad@just.edu.jo

KAZAKSHTAN
S. Sautbekov, sautbek@mail.ru

LITHUANIA
L. Svilainis, linas.svilainis@ktu.lt

RUSSIA
M. Bakunov, bakunov@rf.unn.runnet.ru
A. Grigoriev, adgrigoriev@mail.ru

SERBIA
B. Reljin, ereljin@ubbg.etf.bg.ac.yu

SPAIN
E. Gago – Ribas, egr@tsc.uniovi.es
M. Gonzalez – Morales, gonmor@yllera.tel.uva.es

UNITED KINGDOM
G. Goussetis, G.Goussetis@hw.ac.uk

Publishing Department

M. Georgieva – Grosse, mariana.georgieva-grosse@de.bosch.com
H. Moshovitis, harism@noc.ntua.gr
I. Ouranos, iouranos@central.ntua.gr

Journal of Applied Electromagnetism

Copyright Form

The undersigned I confirm that I agree the publication of the article

in the Journal of Applied Electromagnetism and the copyright to belong to Trans Black Sea Union of Applied Electromagnetism. I understand that I have the full right to reuse this manuscript for my own purposes.

Name:

Surname:

Address:

E-mail:

Signed:

***Please send the previous form signed either by e-mail to pfrangos@central.ntua.gr , or by fax to the fax number: +30 210 772 2281, attention of Prof. P. Frangos.**

Address

Institute of Communication and Computer Systems

National Technical University of Athens

9,Iroon Polytechniou str.,

15773 Athens - GREECE

Tel: (+30) 210772 3694

Fax: (+30) 210772 2281, attention of Prof. P. Frangos

e-mail: pfrangos@central.ntua.gr

Web site: **http://jae.ece.ntua.gr**

TRANS BLACK SEA REGION UNION OF APPLIED ELECTROMAGNETISM (BSUAE)

JOURNAL OF APPLIED ELECTROMAGNETISM (JAE)

Volume 12 Number 3 December 2010

CONTENTS

DEVELOPMENT AND SOLUTION OF THE INTEGRAL EQUATION FOR AXIAL CURRENT OF A CENTER-DRIVEN DIPOLE

K. V. Kotetishvili, G. V. Kekelia, G. Sh. Kevanishvili, I.G. Kevanishvili and B. G. Midodashvili 1

A novel approach to the theory of a dipole is developed. The kernel of the integral equation of the axial current is represented in the analytical form. It consists of two parts–regular and singular, the latter being of the logarithmic kind and having an infinitely large peak. This makes possible to represent the kernel of the equation in the form of the δ-similar function, which determined the transformation of this equation into the second kind Fredholm equation; the solution of the integral equation is given in the analytical form. The comparison of the theoretically obtained values of the axial current with the known experimental data, the agreement of which is rather good, is given.

THE RING STRUCTURE AND RELATIVE POSITION OF MAXIMA OF SOME CHARACTERISTICS OF THE HIGH-FREQUENCY INDUCTION DISCHARGE

A. V. Gerasimov, A. P. Kirpichnikov, O. V. Zelenko 15

On the basis of theoretical analysis of distributions of the conductivity, current density and specific power of heat release in the high-frequency induction discharge, a law of crowding of maxima of these values has been established.

AN ITERATIVE DECODING AND ALGEBRA OF LOG-LIKELIHOOD FUNCTION

N. N. Tashatov 23

Principles of the iterated turbo coding with combination of two or more composite codes have been considered in the article. Also fundamental statistical measures, such as a posterior probability and likelihood, which use for the description of the transfer reliability of the decoder with a soft entry and a soft exit, have been discussed.

AN EOG BASED HUMAN COMPUTER INTERFACE SYSTEM FOR ONLINE CONTROL

C. A. Vinhais, F. A. Santos and J. F. Oliveira **32**

Human to machine interfaces have received more and more attention of researchers in recent years. Electrooculography (EOG) is a new technology to sense eye signals and can be used as an efficient bio-based human computer interface (HCI). The paper is concerned with the design and implementation of an eye movement detection system for biomedical research. The described system includes several electronic units for acquisition, conditioning, amplification and noise filtering of measured voltage signals. Analog to digital conversion of such biopotentials is achieved with an Arduino BT board. With its built-in Bluetooth module, it allows for wireless communication to personal computers for further signal processing and analysis. Experimental results based on real-life EOG signals show that the developed system is efficient in terms of accuracy and applicability. The proposed solution is a low-cost general purpose EOG-based HCI system that can be used by patients with disabilities for communication..

FDTD MODELING OF REFRACTOMETRIC OPTICAL SENSORS BASED ON QUASI-ONE-DIMENSIONAL PHOTONIC CRYSTALS

G. S. Kliros and K. A. Papageorgiou **39**

We report on the design of a refractometric optical sensor based on a quasi-one dimensional photonic crystal structure etched in a Si_3N_4 ridge waveguide grown on top of a SiO_2 substrate. A photonic crystal based on this kind of structure exhibits a photonic bandgap for TE polarized light. The finite difference time domain method (FDTD) is employed in order to design the device and investigate its transmission spectra and sensitivity characteristics. The shift in the central wavelength of the reflectivity spectrum, due to change in the refractive index, when the low-index areas of the photonic crystal are infiltrated with different fluids, is found to be linear and hence, suitable for refractrometric sensing applications.

DEVELOPMENT AND SOLUTION OF THE INTEGRAL EQUATION FOR AXIAL CURRENT OF A CENTER-DRIVEN DIPOLE

K.V. Kotetishvili*, G.V. Kekelia**, G. Sh., Kevanishvili***, I.G., Kevanishvili***, B.G. Midodashvili****,

*Georgian Technical University, Department of Physics,
0175, 77, M. Kostava Str., Tbilisi, Georgia
E-mail: Ketinooo@hotmail.com
**Georgian-Ukrainian Int. University Iberia, Department of Telecommunication
0177, 47, A. Kazbegi Str.,Tbilisi, Georgia
***Georgian Technical University, Faculty of Energetics & Telecommunication,
0175, 77, M. Kostava Str., Tbilisi, Georgia
****I. Javakhishvili Tbilisi State University, Department of Computer Science
0186, 2, University Str., Tbilisi, Georgia

Abstract

A novel approach to the theory of a dipole is developed. The kernel of the integral equation of the axial current is represented in the analytical form. It consists of two parts–regular and singular, the latter being of the logarithmic kind and having an infinitely large peak. This makes possible to represent the kernel of the equation in the form of the δ *-similar function, which determined the transformation of this equation into the second kind Fredholm equation; the solution of the integral equation is given in the analytical form. The comparison of the theoretically obtained values of the axial current with the known experimental data, the agreement of which is rather good, is given.*

1. INTRODUCTION

As is known, the axial current of the hollow active dipole satisfies the following integral equation [1, 4]

$$\int_{-h/2}^{h/2} I(z')K(|z-z'|)dz' = A\cos kz + B\sin(k|z|), \tag{1}$$

where z and z' are the coordinates of two arbitrarily chosen points on the surface of the dipole, h is the length of the dipole: $k = \frac{2\pi}{\lambda}$; λ - the wavelength in vacuum; A - the unknown coefficient; $B = \frac{2\pi V^{(e)}}{i\zeta_0}$; $V^{(e)}$ - the amplitude of the electro-motive-force (e.m.f) applied to the center of the dipole, where $\zeta_0 = 120\pi\ \Omega$, $K(|z-z'|)$ is the kernel of the integral equation given as follows:

$$K(|z-z'|)=\frac{1}{2\pi}\int_0^{2\pi}\frac{\exp\left(-ik\sqrt{4a^2\sin^2\frac{\varphi}{2}+(z-z')^2}\right)}{\sqrt{4a^2\sin^2\frac{\varphi}{2}+(z-z')^2}}d\varphi, \tag{2}$$

where a is the radius of the dipole. Assume that the following strong inequalities $ka<<1$ and $a<<h$ in equation (1) are valid; these conditions tempt to represent integral (2) in the approximate form [4]

$$\tilde{K}(|z-z'|)=\frac{\exp\left(-ik\sqrt{a^2+(z-z')^2}\right)}{\sqrt{a^2+(z-z')^2}}, \tag{3}$$

which has been till very popular till present days.

Mention that there is sufficient difference between expressions (2) and (3) (see below). Here we emphasize the fact that, at the $z'=z$ point, function $K\left(|z-z'|\right)$ has infinitely great break $\left(|K(0)|=\infty\right)$, while $\left(|\tilde{K}(0)|=\frac{1}{a}<\infty\right)$. Since a is small, function $\tilde{K}\left(|z-z'|\right)$ has a very large peak, which, at a definite value, puts it close to peak properties of function $K\left(|z-z'|\right)$.

If the kernel of equation (1) is given by (3), this equation holds the name of Hallen.

There are a lot of analytical and numerical methods of approximate solution of this equation (see, e.g., [2]-[4]). Work [4] also attracts attention due to the presence of physical interpretation and numerical results of the solution of Hallen's equation by the analytical-numerical method, these results are in a very good agreement with the experimental data [5]. However, the theory developed is true only at $\frac{kh}{2}\le\frac{5\pi}{4}$.

In scientific literature, integral (2) has not been presented in the analytical form yet. Thus, the interrelation between functions (2) and (3) is also unknown yet.

Therefore, in order to carry out the correct analysis of integral equation (1), it is necessary at first to represent its kernel (2) in the analytical form and, just in this way, to determine its main properties, which makes possible to reach definite progress in formation of the theory of a dipole.

2. THE STRUCTURE OF THE KERNEL (2)

Consider Green's function presented within integral (2) in the integral form [6]:

$$\frac{\exp\left(-ik\sqrt{4a^2\sin^2\frac{\varphi}{2}+(z-z')^2}\right)}{\sqrt{4a^2\sin^2\frac{\varphi}{2}+(z-z')^2}}=$$

$$=\int_0^\infty \frac{\exp\left(-i\,|z-z'|\sqrt{x^2-k^2}\right)\cdot xJ_0\left(2xa\sin\psi\right)}{\sqrt{x^2-k^2}}dx=$$

$$=-ik\int_0^1 \frac{\exp\left(-i\,|z-z'|\sqrt{1-t^2}\right)\cdot tJ_0\left(2kta\sin\psi\right)}{\sqrt{1-t^2}}dt+$$

$$+k\int_1^\infty \frac{\exp\left(-k\,|z-z'|\sqrt{t^2-1}\right)\cdot tJ_0\left(2kta\sin\psi\right)}{\sqrt{t^2-1}}dt,\quad \left(\psi=\varphi/2\right). \tag{4}$$

Substituting this expression into (2) and using the relation given in [6], we have

$$J_0\left(2kta\sin\psi\right)=\sum_{S=-\infty}^{\infty}J_S^2\left(kta\right)\exp\left(i2S\psi\right),$$

$$\int_0^\pi J_0\left(2kta\sin\psi\right)d\psi=\pi J_0^2\left(kta\right),$$

we get

$$K\left(|z-z'|\right)=-ikK_1\left(k\,|z-z'|\right)+kK_2\left(|z-z'|\right), \tag{5}$$

where

$$K_1\left(|z-z'|\right)=\frac{i}{k}\cdot\frac{\exp\left(-ik\,|z-z'|\right)-1}{|z-z'|}, \tag{6}$$

$$K_2\left(|z-z'|\right)=\frac{2}{\pi\sqrt{4\varepsilon^2+k^2\left(z-z'\right)^2}}\cdot$$

$$\left[a_0-b_0\Phi\left(\varepsilon,k\,|z-z'|\right)-2\ln\left(\frac{k\,|z-z'|}{\sqrt{8}\varepsilon}\right)\right],\ \left(\varepsilon=ka<<1\right), \tag{7}$$

where

$$\Phi\left(\varepsilon,k\,|\,z-z'\,|\right)=\ln\left[\frac{8\varepsilon^2}{k^2\left(z-z'\right)^2}\left(1-\frac{2\varepsilon}{\left(4\varepsilon^2+k^2\left(z-z'\right)^2\right)^{1/2}}\right)\right].$$

When deriving this expression, we used the following relations:

$$J_0\left(\varepsilon\sqrt{1+\tau^2}\right)\cong J_0\left(\varepsilon\tau\right)J_0\left(\varepsilon\right)+2\sum_{S=1}^{\infty}(-1)^S J_{2S}\left(\varepsilon\right)J_{2S}\left(\varepsilon\tau\right),$$

$$0\le\tau\le\infty,\quad \varepsilon<<1,$$

$$\int_0^{\infty}\exp\left(-k\,|\,z-z'\,|\,\tau\right)J_0^2\left(\varepsilon\tau\right)d\tau=$$

$$=\frac{2}{\pi\sqrt{4\varepsilon^2+k^2(z-z')^2}}K_0\left(\frac{2\varepsilon}{\sqrt{4\varepsilon^2+k^2(z-z')^2}}\right),$$

where $K_0\left(t\right)$ is the complete ellipse function given by the following polynomial [7]:

$$K_0(t)=(a_0+a_1t_1+a_2t_1^2)-(b_0+b_1t_1+b_2t_1^2)\ln t_1+\mu(t)\,, \tag{8}$$

where

$$t_1=1-t,\ t=\frac{2\varepsilon}{\sqrt{4\varepsilon^2+k^2(z-z')^2}},\ a_0=1.3862944\,,$$

$a_1=0.1119723,\ a_2=0.0725296,\ b_0=0.5,\ b_1=0.1213478,\ b_2=0.0288729,\ \mu(t)\le10^{-3}.$

Since ε is small, expression (7) may be replaced by it's approximate one:

$$K_0(t)\approx a_0-b_0\ln t_1+0(\varepsilon)\,.$$

Substituting expression (5) into (1), we pass on to nondimensional quantities:

$$\xi=\frac{2}{h}z',\eta=\frac{2}{h}z,\beta=k\frac{h}{2}=\pi\frac{h}{\lambda},\omega(\xi)=I(z')\big|_{z'=\frac{h}{2}\xi}. \tag{9}$$

Then, instead of (1) we have:

$$\int_{-1}^{1}\omega\left(\xi\right)T_1\left(|\,\xi-\eta\,|\right)d\xi+\beta\int_{-1}^{1}\omega\left(\xi\right)T_2\left(|\,\xi-\eta\,|\right)d\xi=$$

$$= A\cos\beta\eta + B\sin\beta|\xi|, \tag{10}$$

where

$$T_1(|\xi-\eta|) = \frac{\exp(-i\beta|\xi-\eta|)-1}{|\xi-\eta|} + \frac{\exp(-\beta|\xi-\eta|)-1}{|\xi-\eta|}, \tag{11}$$

$$T_2(|\xi-\eta|) = \frac{2}{\pi\sqrt{4\varepsilon^2+\beta^2(\xi-\eta)^2}}\cdot$$

$$\cdot\left\{a_0 + b_0\left[\Phi(\varepsilon,\beta|\xi-\eta|) - 2\ln(\gamma\beta|\xi-\eta|)\right]\right\}; \tag{12}$$

$$\gamma = \frac{1}{\sqrt{8}\varepsilon}.$$

Further, we shall call (10) a modernized integral equation (MIE) of the dipole.

Now we have the possibility to compare functions $K(|z-z'|)$ and $\tilde{K}(|z-z'|)$. Expression (5) illustrates the sufficient difference between functions $K(|z-z'|)$ and $\tilde{K}(|z-z'|)$ both quantitatively and qualitatively. Mention that function $K(|z-z'|)$ (i.e. the real kernel) consists of the regular $K_1(|z-z'|)$ and singular $K_2(|z-z'|)$ parts. Equation (7) shows that this singularity is of a clear logarithmic kind, while function $\tilde{K}(|z-z'|)$ has no such singularity. The only property approaching $\tilde{K}(|z-z'|)$ to $K(|z-z'|)$ in its behavior is that it has a very high peak at the $z'=z$ point.

Before we pass on to construction of the approximate solution of the MIE, let us set one substantial remark, which we shall use further.

Kernel $T(|\xi-\eta|) = T_1(|\xi-\eta|) + \beta T_2(|\xi-\eta|)$ of the integral equation is determined within the square $(-1 \le \xi,\eta \le 1)$, being zero outside it. Therefore, if we introduce variable $\tau = \xi-\eta$, changing within interval $-2 \le \tau \le 2$, function $T(|\tau|)$ becomes finite, i.e.,

$$T(|\tau|) = \begin{cases} 0, \ when\ |\tau| > 2 \\ T_1(|\tau|) + \beta T_2(|\tau|), \ when\ |\tau| \le 2 \end{cases}$$

Since this function has the infinitely great break at the $\tau = 0$ point, thus, using King's well-known idea [4] that in this case the kernel of equation (1) must be the δ-similar function, we can write:

$$T_2(|\tau|) \approx Q\delta(\tau), \tag{13}$$

where coefficient Q is determined from the normalization condition:

$$Q = \int_{-\infty}^{\infty} T_2(|\tau|)d\tau = \int_{-2}^{2} T_2(|\tau|)d\tau =$$

$$= \frac{2}{\pi}\int_{-2}^{2}\left\{a_0 + b_0\left[\Phi\left(\varepsilon,\beta|\tau|\right) - 2\ln\left(\gamma\beta|\tau|\right)\right]\right\}\frac{d\tau}{\sqrt{4\varepsilon^2 + \beta^2|\tau|^2}} =$$

$$= \frac{1}{\pi\beta}\left[12.875\ln^2\left(\frac{2\beta}{\varepsilon}\right) - \left(8\ln(4\beta) - 2.76\right)\ln\left(\frac{2\beta}{\varepsilon}\right)\right]. \tag{14}$$

3. SOLUTION OF THE INTEGRAL EQUATION

According to (13) equation (10) can be rewritten as follows

$$\omega(\eta) + \mu\int_{-1}^{1}\omega(\xi)T_1(|\xi-\eta|)d\xi = A^*\cos\beta\eta + B^*\sin(\beta|\eta|), \tag{15}$$

where

$$A^* = A/\beta Q,\ B^* = B/\beta Q,\ \mu = 1/\beta Q. \tag{16}$$

Before finding the solution of this equation, let us make some useful remarks: introduce auxiliary function $T_1(|\tau|)$, where $\tau = |\xi - \eta|$, which varies within closed interval $-2 \le \tau \le 2$ and is finite in this interval, i.e., $T_1(|\tau|) \ne 0$ for $|\tau| \le 2$ and $T_1(|\tau|) \equiv 0$ for $|\tau| > 2$. Besides, due to (11) it is continuous within this interval.

Therefore, in view of the Dirichlet well-known theorem [8] it can be expanded into to the Fourier series with respect to cosines, i.e.

$$T_1(|\tau|) = \sum_{s=0}^{\infty} X_s\cos(\pi s\tau), \tag{17}$$

where X_s are the Fourier coefficients being defined by standard formula

$$X_s = \mu_s\int_{-2}^{2} T_1(|\tau|)\cos(\pi s\tau)d\tau, \tag{18}$$

$$\mu_s = \begin{cases} 1/2, \ when \ s = 0 \\ 1, \ when \ s \geq 1 \end{cases}$$

For $s = 0$, from (18) due to (11) we have

$$X_0 = \frac{1}{2}\left\{ \int_{-2}^{2} \frac{e^{-i\beta|\tau|} - 1}{|\tau|} d\tau + \int_{-2}^{2} \frac{e^{-\beta|\tau|} - 1}{|\tau|} d\tau \right\}.$$

Therefore, we received table integrals [7], and finally we have

$$X_0 = \sum_{n=1}^{\infty} \frac{(-1)^n (2\beta)^{2n}}{(2n)(2n)!} + \sum_{n=1}^{\infty} \frac{(2\beta)^n}{n\,n!} + i \sum_{n=0}^{\infty} \frac{(-1)^n (2\beta)^{2n+1}}{(2n+1)(2n+1)!} \ . \tag{19}$$

The value of the integral (18), when $s \geq 1$, can be calculated due to the well-known quadrature [9] (see appendix)

$$X_s = -4 f(2) \frac{\sin\beta}{4\pi^2 s^2 - \beta^2} \ . \tag{20}$$

Further, let us receive the approximate, but still correct, solution of integral equation (15) in the analytical form. Since $\tau = \xi - \eta$, then in view of (17) we have

$$T_1(|\xi - \eta|) = \sum_{s=0}^{\infty} X_s \left[\cos(\pi s \xi)\cos(\pi s \eta) + \sin(\pi s \xi)\sin(\pi s \eta) \right],$$

which, being substituted into (15), gives the following functional equation

$$\omega(\eta) + \mu \sum_{s=0}^{\infty} X_s x_s \cos(\pi s \eta) = A^* \cos\beta\eta + B^* \sin(\beta|\eta|), \tag{21}$$

where

$$x_s = \int_{-1}^{1} \omega(\xi)\cos(\pi s \xi) d\xi \, . \tag{22}$$

Since $\omega(\xi)$ is an unknown function, then it is clear that x_s $(s = 0,1,2,...)$ represents a sequence of unknown values too; they must be determined by the functional equation (21). According to the Fourier's inverse theorem from (22) we have

$$\omega(\xi) = \sum_{s=0}^{\infty} \varepsilon_s x_s \cos(\pi s \xi), \tag{23}$$

$$\varepsilon_s = \begin{cases} 1, \ when \ s = 0 \\ 2, \ when \ s \geq 1 \end{cases}$$

Substitution of (23) into the left side of (21) gives the following equation

$$\sum_{s=0}^{\infty} x_s(\varepsilon_s + \mu X_s)\cos(\pi s\eta) = A^* \cos\beta\eta + B^* \sin(\beta\,|\,\eta\,|), \tag{24}$$

which solution is

$$x_s = \frac{A^* a_s + B^* b_s}{1 + \mu\lambda_s X_s}, \ (\lambda_s = 1/\varepsilon_s), \tag{25}$$

where

$$a_s = \int_{-1}^{1} \cos(\beta\eta)\cos(\pi s\eta)d\eta = 2\frac{(-1)^{s+1}}{\pi^2 s^2 - \beta^2}\beta\sin\beta, \tag{26}$$

$$b_s = \int_{-1}^{1} \sin(\beta\,|\,\eta\,|)\cos(\pi s\eta)d\eta = 2\beta\frac{\left[1 - (-1)^s\cos\beta\right]}{\pi^2 s^2 - \beta^2}. \tag{27}$$

Further, substitute (25) into (21) and represent the received result in the form

$$\omega(\eta) = -\left\{A^*\left[\cos\beta\eta - \mu\bar{a}_0 R(\beta)\right] + B^*\left[\sin(\beta\,|\,\eta\,|) - \mu\bar{b}_0 R(\beta)\right]\right\}, \tag{28}$$

where

$$\bar{a}_0 = \frac{a_0 X_0}{1 + \mu X_0}, \qquad \bar{b}_0 = \frac{b_0 X_0}{1 - \mu X_0}, \tag{29}$$

$$F_1(\beta,\eta) = \sum_{s=1}^{\infty}\frac{X_s a_s \cos(\pi s\eta)}{1 + \mu X_s/2}, \quad F_2(\beta,\eta) = \sum_{s=1}^{\infty}\frac{X_s b_s \cos(\pi s\eta)}{1 + \mu X_s/2}. \tag{30}$$

After determining the unknown coefficient A^* from the condition $\omega(\pm 1) = 0$ we receive

$$A^* = -B^*\frac{\sin\beta - \mu x - \mu F_2(\beta,1)}{\cos\beta - \mu æ - \mu F_1(\beta,1)}. \tag{31}$$

By substitution of the latter expression into (28) and some algebraic transformations we obtain a unique solution of the integral equation (15)

$$\omega(\eta) = -\frac{B^*}{\Delta(\beta)}\{\sin[\beta(1-|\eta|)] - \mu x(\cos\beta\eta - \cos\beta) + \mu æ(\sin\beta|\eta| - \sin\beta) -$$

$$-\mu[F_2(\beta,1)\cos\beta\eta - F_2(\beta,\eta)\cos\beta] - \mu^2 æ[F_2(\beta,1) - F_2(\beta,\eta)] +$$

$$+\mu^2[F_1(\beta,\eta)F_2(\beta,1) - F_1(\beta,1)F_2(\beta,\eta)]\}, \qquad (32)$$

where

$$\Delta(\beta) = \cos\beta - \mu æ - \mu F_1(\beta,1)\,. \qquad (33)$$

4. CALCULATION OF FUNCTIONS $F_1(\beta,\eta)$ AND $F_2(\beta,\eta)$

These functions are represented by series (30). According to (20) and (26), when $\mu X_s \ll 1$, we have approximate equality

$$F_1(\beta,\eta) = -\frac{4\beta^2}{\pi^2}\sin^2\beta\cos\beta\sum_{s=1}^{\infty}\frac{(-1)^s\cos(xs)}{(s^2-a^2)^2}, \qquad (34)$$

where we use the following notations $x = \pi\eta$ and $a = \beta/\pi$. The series

$$S_1(\beta,\eta) = \sum_{s=1}^{\infty}\frac{(-1)^s\cos(xs)}{(s^2-a^2)^2}$$

is well-known (see, e.g. [6], p. 731); its sum equals

$$S_1(\beta,\eta) = -\frac{\pi^4}{4\beta^4} + \frac{\pi^4}{4\beta^4}\sin\beta\cos\beta\eta + \pi(1+|\eta|)\sin\beta + \frac{\pi^4}{2\beta^2}\cos[\beta(1+|\eta|].$$

Therefore, the expression (34) takes the form

$$F_1(\beta,\eta) = -\sin^2\beta\cos\beta\{2 - [\beta\cos\beta\eta\sin\beta + \beta(1+|\eta|) - \beta^2\sin\beta\cos\beta(1+|\eta|)]\}.$$

Analogously, we have

$$F_2(\beta,\eta) = -\sin 2\beta\{-2 + \beta\sin 2\beta[\sin\beta\cos\beta(1-|\eta|) - \beta\eta\sin(\beta(1-|\eta|))] +$$

$$+\sin\beta\sin 2\beta\cos\beta + \beta\sin^2 2\beta S_1(\beta,\eta)\frac{4}{\pi^2}\}.$$

5. ANALYSIS OF THE RESULT

The expression (32) explicitly describes the law of distribution of axial current of a dipole in the analytical form. It has a certain physical meaning: the term

$$\omega_1(\eta) = -\frac{B^*}{\Delta(\beta)}\sin\left[\beta\left(1-|\eta|\right)\right], \tag{35}$$

corresponds to a standing sinusoidal current wave on the surface of a dipole, which exists due to the electromotive force in the center of a dipole. The other terms, which are proportional to μ and μ^2, describe standing waves of complex structure; they are induced by the electromagnetic (interferential) interaction of the upper and lower sides of a dipole.

The intensity of these waves depends on the numerical value of the parameter μ (see (16) and (14)), it is clear that for small values of the electrical radius of a dipole $\varepsilon = ka = 2\pi a/\lambda$ the value of the parameter μ is small too (in practical cases the value of a/λ varies within $6\cdot 10^{-4} \le a/\lambda \le 7\cdot 10^{-3}$); therefore, for construction of the diagram of a dipole radiation we can use the formula (34) instead of (32), but it is useless for calculation of the admittance of a dipole $Z_i = V^{(e)}/\omega(0)$ since in this case $\omega(0) = -B^*\sin\beta/\Delta(\beta)$, while $B^* = -i2\pi V^{(e)}/\varsigma_0$, where $V^{(e)}$ is the amplitude of electromotive force applied at the center of a dipole, $\varsigma_0 = 120\pi\,\Omega$, and, therefore, the admittance does not have a real part, that does not correspond to the reality. Because of the smallness of the parameter μ it is acceptable to use the following approximate relationship instead of (35)

$$\omega(\eta) \cong -\frac{B^*}{\Delta(\beta)}\{\sin[\beta(1-|\eta|)] - \mu x(\cos\beta\eta - \cos\beta) + \mu æ(\sin\beta|\eta| - \sin\beta)\,. \tag{36}$$

Since $\eta = \frac{2}{h}z'$, $\omega(\eta) = J(z')$, where z' represents the coordinate of a point of observation located on the surface of a dipole and $J(z')$ is the axial current, then instead of (36) we have

$$J(z') = A\left\{\sin\left[2\pi\left(\frac{h}{2\lambda} - \frac{|z'|}{\lambda}\right)\right] - \mu x\left[\cos\left(\frac{2\pi z'}{\lambda}\right) - \cos\left(\pi\frac{h}{\lambda}\right)\right] + \right.$$

$$\left. + \mu æ\left[\sin\left(\frac{2\pi|z'|}{\lambda}\right) - \sin\left(\pi\frac{h}{\lambda}\right)\right]\right\}, \tag{37}$$

$$A = B^* / \Delta(\beta) = 2\pi i V^{(e)} / \beta Q \varsigma_0 .$$

By use of this formula, below we give the diagrams of norm current $J_{nor} = | J(z') / V^{(e)} | \left(\frac{mA}{v} \right)$ for the cases $\varepsilon = 0.044$, $h/\lambda = 0.5$; $h/\lambda = 0.75$; $h/\lambda = 1$; $h/\lambda = 1.25$. By dotted curves are denoted the results obtained by experiments [4, 5]. As it is clear from the diagrams, the values received by theoretical approach and by experiments are in good concordance.

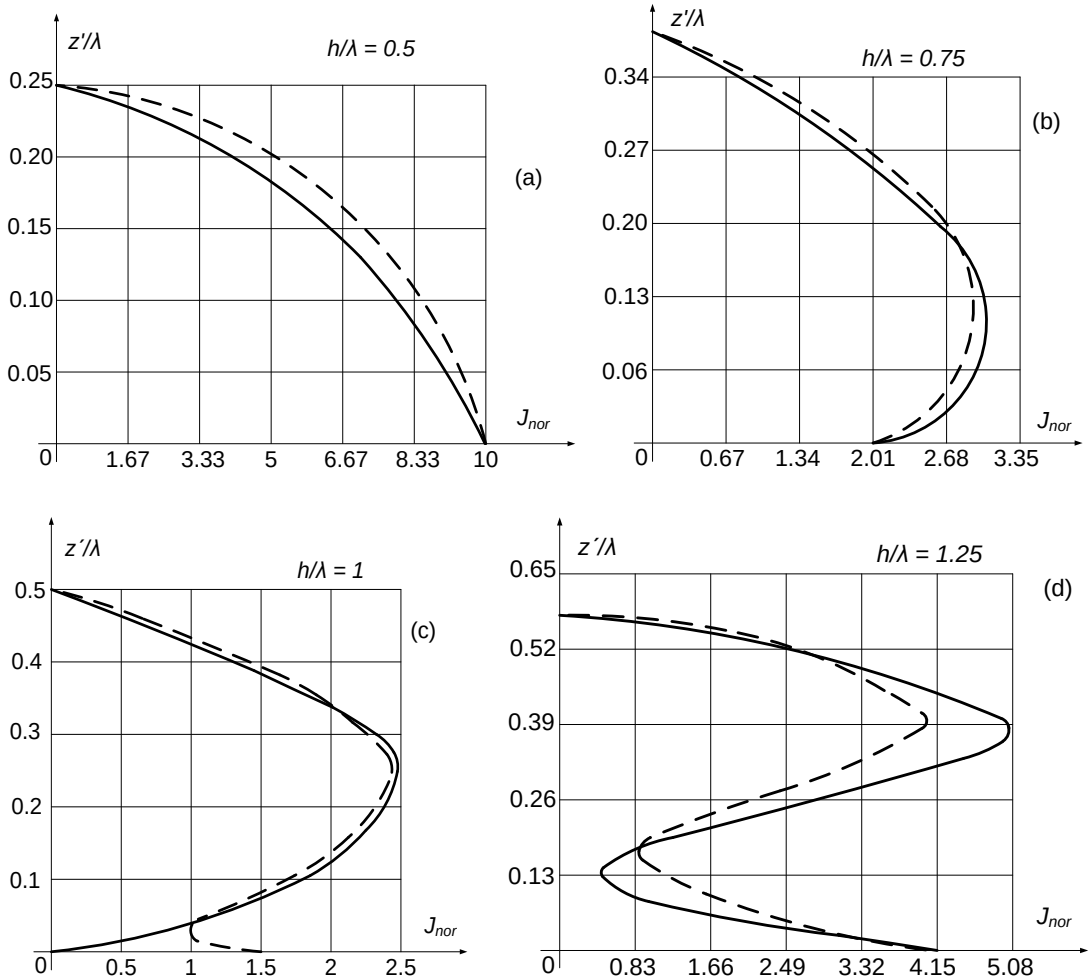

Fig. 1 Dependence of the modulus of the axial current on z'/λ for different values of h/λ

4. CONCLUSION

In this paper, the integral equation of a dipole with respect to the axial current is solved in approximate, analytical form with accuracy $O(\mu^2)$, $(\mu \ll 1)$; from the physical point of view the solution represents a superposition of the standing waves along a dipole with certain physical meanings.

The law of distribution of the current theoretically obtained by us is in good concordance with the results obtained experimentally by others, which confirms the validity of the theory we offered.

APPENDIX. DERIVATION OF THE FORMULA (20)

Taking into account (11) from (20) we receive

$$X_s = \int_{-2}^{2} \left(e^{-i\beta|\tau|} + e^{-\beta|\tau|} - 2 \right) \cos \pi s \tau \frac{d\tau}{|\tau|} \tag{I}$$

Using notation

$$\varphi(\tau) = \left(e^{-i\beta|\tau|} + e^{-\beta|\tau|} - 2 \right) \Big/ |\tau| \tag{II}$$

and taking into account that $\cos \pi s \tau = \frac{1}{2}\left(e^{i\pi s\tau} + e^{-i\pi s\tau} \right)$, the expression (I) can be rewritten as follows

$$X_s = \frac{1}{2} X_s^{(1)}(\beta) + \frac{1}{2} X_s^{(2)}(\beta), \tag{III}$$

where we use notations

$$X_s^{(1)}(\beta) = \int_{-2}^{2} \varphi(\tau) e^{i\pi s\tau} d\tau, \tag{IV}$$

$$X_{-s}^{(1)}(\beta) = \int_{-2}^{2} \varphi(\tau) e^{-i\pi s\tau} d\tau. \tag{V}$$

In view of (II) the integrand of (IV) can be represented as follows

$$\varphi(\tau) e^{i\pi s\tau} = e^{i\left(\pi s - \frac{\beta}{2}\right)|T|} f(\tau),$$

where

$$f(\tau) = \left(e^{-i\frac{\beta}{2}|T|} + e^{-\left(\beta - i\frac{\beta}{2}\right)|T|} - 2e^{i\frac{\beta}{2}|T|} \right) \Big/ |T|. \tag{VI}$$

Therefore, (IV) can be rewritten as follows

$$X_s^{(1)}(\beta) = \int_{-2}^{2} e^{i\omega_s|\tau|} f(\tau) d\tau, \quad \omega_s = \left(\pi s - \frac{\beta}{2}\right). \qquad \text{(VII)}$$

Since $f(\tau)$ is continuous function in the closed segment $[-2,\ 2]$, then for the integral (VII) we can use the Bakhvalov quadrature [9], according to which we receive

$$X_s^{(1)}(\beta) = 2[D_1(P_s) f(-2) + D_2(P_s) f(2)], \quad f(-2) = f(2),$$

where

$$P_s = 2\omega_s = 2\pi s - \beta, \ D_{1,2}(P_s) = \frac{\sin P_s}{P_s} \pm i \frac{P_s \cos P_s - \sin P_s}{P_s^2},$$

i.e.

$$X_s^{(1)}(\beta) = 4 f(2) \frac{\sin P_s}{P_s} = -4 f(2) \frac{\sin \beta}{2\pi s - \beta}.$$

It is obvious that according to (V)

$$X_{-s}^{(1)}(\beta) = 4 f(2) \frac{\sin \beta}{2\pi s + \beta}.$$

Therefore, taking into account (III), finally we have

$$X_s(\beta) = -4 f(2) \frac{\sin \beta}{4\pi^2 s^2 - \beta^2}.$$

This research was performed in part under supporting of the Grant #4390 of The Science and Technology Center in Ukraine (STCU). The authors would like to thank STCU for financial support.

REFERENCES

[1] T.T. Wu, “Introduction to Linear Antennas”, in Antenna Theory, Part 1, ed. by R.E. Collin and F.J. Zucker, p.321, (New York, McGraw – Hill, 1969).

[2] G. Fikioris and Tai Tsun Wu, “On the Application of Numerical Methods to Hallen’s Equation”, IEEE Trans., Antennas Propagation, March2001, vol. 49, No 3, pp. 383-392.

[3] A.N. Tikhonov, A.S. Ilinski and A.G. Sveshnikov, “Mathematical Models of Electrodynamics of Radiating Systems”, in Problems of Calculating Techniques.- Moscow, MSU, 1980, p. 96 (in Russian).

[4] R.W.P. King and G.S. Smith, “Antennas”, in Matter. – the MIT PRESS, England, 1961.

[5] R.B. Mack, “A Study of Circular Arrays”, II and III, Tech. Repts, 382, 383. – Cruft Laboratory, Harvard University, Cambridge, Mass., 1063.

[6] A.P. Prudnikov, I.A. Brichkov and O.I. Marichev, “Integrals and Series (Special Functions)”, Moscow, Nauka, 1983, (in Russian).

[7] M. Abramowitz and I.A. Stegun, “Handbook of Mathematical Functions”, National Bureau of Standards, Appl. Math. Ser. 55, Issued June 1964.

[8] V.I. Smirnov, “The course of High Mathematics, v. II”, Moscow, Gostekhizdat, 1943, p. 399 (in Russian).

[9] N.S. Bakhvalov, N.P. Jidkov and G.M. Kobelkov, “Numerical methods”, Moscow “Nauka”, 1987, p. 115 (in Russian).

THE RING STRUCTURE AND RELATIVE POSITION OF MAXIMA OF SOME CHARACTERISTICS OF THE HIGH-FREQUENCY INDUCTION DISCHARGE

Alexander V. Gerasimov, Alexander P. Kirpichnikov, Olga V. Zelenko

Kazan State Technological University, 420015, Karl Marx str., 68 Kazan, Russia
e-mail: gerasimov@kstu.ru

Abstract

On the basis of theoretical analysis of distributions of the conductivity, current density and specific power of heat release in the high-frequency induction discharge, a law of crowding of maxima of these values has been established.

1. INTRODUCTION

In electro-plasma processes and power plants using high-frequency induction (HFI) plasma, the discharge zone is the main process zone. Information on distribution of main parameters of the discharge (conductivity, temperature, current density, specific power of heat release) and position of maxima of these values gives an opportunity to determine optimal conditions for heating the initial material and to manufacture a high-quality product.

The results of experimental works [1]-[3] allowed us to suggest that for each section inside a plasmoid of the HFI discharge, the following inequality holds true

$r_1<r_2<r_3,$ (1)

where $r_1=r(\sigma_{max})$, $r_2=r(j_{\varphi\ max})$ and $r_3=r(W_{max})$ are the radial coordinates corresponding to the maxima of physical quantities within the parentheses.

In these relations σ is the conductivity of the discharge, $j=\sigma E_\varphi$ is the eddy current density, E_φ is the strength of the azimuth electric field, and $W=\frac{1}{2}\sigma E_\varphi^2$ is the power input to the discharge per unit volume averaged over a period of the high-frequency field.

Figure 1 shows dependences of the conductivity of the discharge σ(r), eddy current density $j=\sigma E_\varphi$, bulk density of the power input to the discharge $W=\frac{1}{2}\sigma E_\varphi^2$ in various sections of a HFI plasmoid, starting from its central section downstream and illustrating the relation (1). The results are obtained on a stationary semi-commercial unit HFI-11/60 using a procedure described in Refs. [1-3].

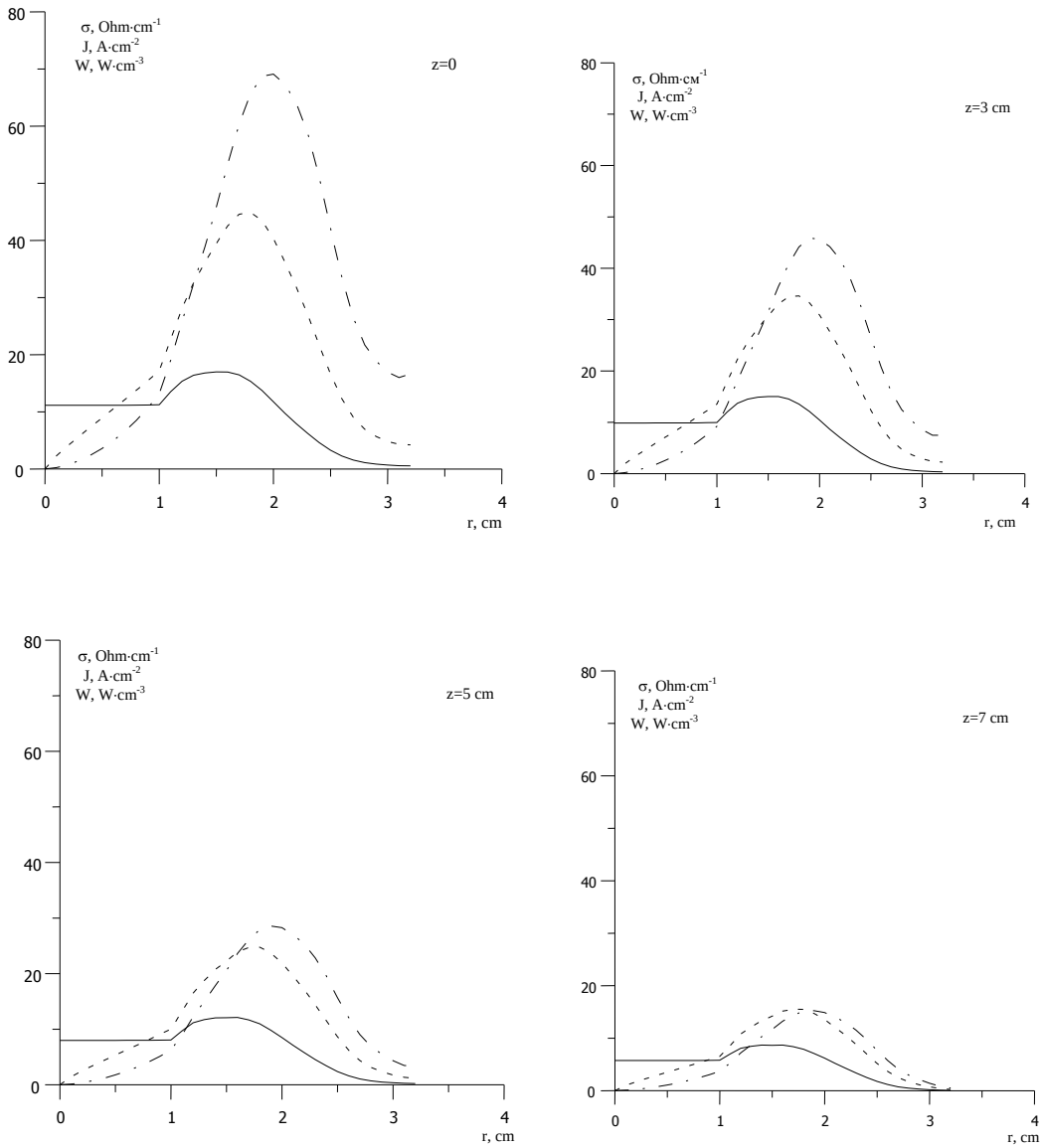

Figure 1 Radial distribution of conductivity σ - ____, eddy current density j - - - - and heat power W -·-·-·- for various cross-section of the plasmoid

2. THEORETICAL PART

Inequality (1) can be analytically proven as follows.

Let us assume that the conductivity of the discharge σ(r,z), current density $j_\varphi(r,z)=\sigma E_\varphi$ and power of heat release $W=\frac{1}{2}\sigma E_\varphi^2$ are the functions, which at each fixed section of the discharge reach their maximum values only once on the interval $0 \le r \le R$. One may prove that in this case the relation $r(\sigma_{max}) < r(j_{\varphi max}) < r(W_{max})$ holds true.

At the point $r_1 = r(\sigma_{max})$

$$\left.\frac{\partial\sigma(r)}{\partial r}\right|_{r_1} = 0,$$

so

$$\frac{\partial\sigma(r)}{\partial r} > 0 \text{ when } r < r_1,$$

and

$$\frac{\partial\sigma(r)}{\partial r} < 0 \text{ when } r > r_1.$$

Then at the point $r_2 = r(j_{\varphi max})$ we have

$$\left.\frac{\partial(\sigma E_\varphi)}{\partial r}\right|_{r_2} = \left.\frac{\partial\sigma}{\partial r}\right|_{r_2} E_\varphi(r_2) + \sigma(r_2)\left.\frac{\partial E_\varphi}{\partial r}\right|_{r_2} = 0.$$

Since $E_\varphi(r), \sigma(r), \frac{\partial E_\varphi(r)}{\partial r}$ are nonnegative values in the whole volume of a discharge, at the point r_2

$$\left.\frac{\partial\sigma}{\partial r}\right|_{r_2} = -\frac{\sigma(r_2)}{E_\varphi(r_2)}\left.\frac{\partial E_\varphi}{\partial r}\right|_{r_2} < 0,$$

and this means that the point $r_2 = r(j_{\varphi\max})$ is situated at the descending path of the function $\sigma(r)$, i.e., on the interval $r_1 < r < R$. Therefore, $r_2 > r_1$.

At the point $r_3 = r(W_{max})$, in turn, we have:

$$\left.\frac{\partial(\sigma E_\varphi^2)}{\partial r}\right|_{r_3} = \left.\frac{\partial(\sigma E_\varphi)}{\partial r}\right|_{r_3} E_\varphi(r_3) + \sigma(r_3)E_\varphi(r_3)\left.\frac{\partial E_\varphi}{\partial r}\right|_{r_3} = 0.$$

Hence

$$\left.\frac{\partial(\sigma E_\varphi)}{\partial r}\right|_{r_3} = -\sigma(r_3)\left.\frac{\partial E_\varphi}{\partial r}\right|_{r_3} < 0,$$

and, consequently, $r_3 > r_2$.

Finally we obtain the relation $r_1 < r_2 < r_3$, which was to be proven.

Thus, one may state that inside the HFI discharge the radial coordinates corresponding to maximum values of the conductivity, eddy current density and power input to the discharge are arranged in increasing order.

Note that using the method applied one can prove a more general result,

$$r_1 < r_2 < ... < r_i ... < r_n, \qquad (2)$$

where $r_i = r\left[\left(\sigma E_\varphi^{i-1}\right)_{\max}\right]$; i=1, 2,…, n, and n is integer number that can be made as large as is wished. Inequality (1) is particular case of (2). Therefore, there is a set coaxial cylindrical surfaces inside an HFI discharge that correspond to the maximus of σE_φ^{i-1}.

Under conditions of local thermodynamic equilibrium, the surface of minimum radius $r_1 = r(\sigma_{\max})$ of the set of surfaces (2) corresponds to the maximal temperature $T_{\max} = T(r_1)$ inside the plasmoid, because the relationship $\sigma = \sigma(T)$ between the temperature and the conductivity of the discharge is unambiguous in this case.

3. CALCULATED PROCEDURE

Let us find a law of crowding of r_i points corresponding to maxima of the σE_φ^{i-1} (i=1, 2, 3) values on the r-axis in the direction of the plasmoid periphery, that is first three points r_1, r_2, and r_3, most interesting to technical applications.

Let us examine the function of the form

$$y_i = \sigma E_\varphi^{i-1}.$$

The changes of the E_φ value can be approximated by a straight line

$$E_\varphi = a \cdot r^{i-1},$$

while the σ value is chosen in the form

$$\sigma = \sigma_{max} \cdot e^{-\left(\frac{r-r_0}{\Delta r}\right)^2}.$$

Then

$$y = a \cdot r^{i-1} \cdot \sigma_{max} \cdot e^{-\left(\frac{r-r_0}{\Delta r}\right)^2}.$$

In this case, from mathematical point of view, the problem of finding maxima of σE_φ^{i-1} values as a function of the radial coordinate r reduces to the problem of finding maxima of the following function

$$y = a \cdot r^{i-1} \cdot \sigma_{max} \cdot e^{-\left(\frac{r-r_0}{\Delta r}\right)^2}, \qquad i=1, 2, 3$$

which can be solved by standard methods of applied analysis.

For the point $r^* = r(f_{max})$, apparently, we have the relation

$$\frac{\partial\left(ar^{i-1}e^{-\left(\frac{r-r_0}{\Delta r}\right)^2}\right)}{\partial r} = a(i-1)r^{i-2}e^{-\left(\frac{r-r_0}{\Delta r}\right)^2} - a \cdot r^{i-1} \cdot \frac{2(r-r_0)}{\Delta r^2} e^{-\left(\frac{r-r_0}{\Delta r}\right)^2} = 0$$

or

$$(i-1)r^{i-2} - r^{i-1} \cdot \frac{2(r-r_0)}{\Delta r^2} = 0,$$

so

$$r^2 - r \cdot r_0 - (i-1) - \frac{(\Delta r)^2}{2} = 0 .$$

The solution of this quadratic equation can be written as

$$r_{1,2} = \frac{r_0 \pm \sqrt{r_0^2 + 2(i-1)(\Delta r)^2}}{2}$$

or

$$r_{1,2} = \frac{r_0 \pm r_0 \sqrt{1 + 2(i-1)\left(\frac{\Delta r}{r_0}\right)^2}}{2} .$$

On physical grounds the positive sign should be used

$$r^* = \frac{r_0}{2}\left(1 + \sqrt{1 + 2(i-1)\left(\frac{\Delta r}{r_0}\right)^2}\right).$$

At i=i+1

$$\tilde{r}^* = \frac{r_0}{2}\left(1 + \sqrt{1 + 2i\left(\frac{\Delta r}{r_0}\right)^2}\right).$$

That is

$$\Delta = \tilde{r}^* - r^* = \frac{r_0}{2}\left(1 + \sqrt{1 + 2i\left(\frac{\Delta r}{r_0}\right)^2}\right) - \frac{r_0}{2}\left(1 + \sqrt{1 + 2(i-1)\left(\frac{\Delta r}{r_0}\right)^2}\right) =$$

$$= \frac{\sqrt{1 + 2i\left(\frac{\Delta r}{r_0}\right)^2} - \sqrt{1 + 2(i-1)\left(\frac{\Delta r}{r_0}\right)^2}}{2} .$$

When $i \to \infty$, $\tilde{r}^*(i) - r^*(i-1) \to 0$ or $\tilde{r}^* \approx r^*$, i.e. the points corresponding to maxima of the σE_{φ}^{i-1} values, should crowd.

4. RESULTS AND CONCLUSIONS

Let us estimate the value of this crowding. The estimation procedure is illustrated in Figure 2.

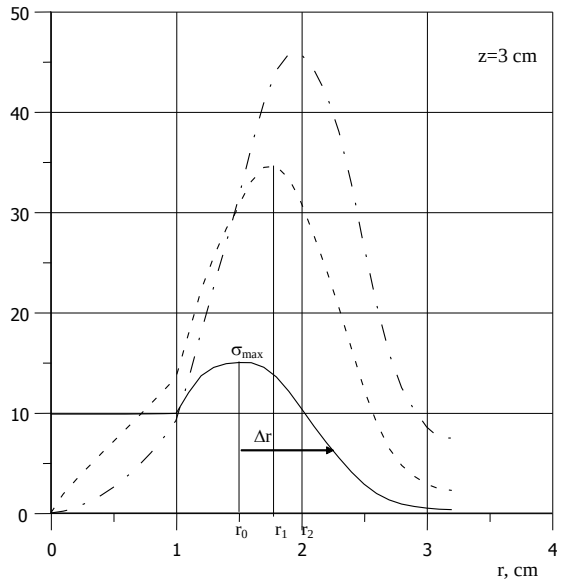

Figure 2 Illustration of a technique of an estimation of value of a crowding

The point $r_0(\sigma_{max})$ corresponding to the maximum of the conductivity value σ is chosen on the plot. In our case, σ_{max}=15.0. The radial coordinate r_0 corresponding to σ_{max} is 1.5 cm. Then a standard half-width of an exponential curve Δr is determined, i.e. at this point the value σ is diminished e-fold from σ_{max}. In our case, Δr=0.8 cm. Then $\frac{\Delta r}{r_0} = \frac{0,8}{1,5} = 0,53$.

Let us estimate the Δ values for the j and W values denoting them as Δ_1 and Δ_2, respectively. As one may see from the figure, $\Delta_1=r_1-r_0$ and $\Delta_2=r_2-r_1$.

$$\Delta_1 = 1,5 \cdot \frac{\sqrt{1+2\cdot 1\cdot (0,53)^2}-1}{2} = 0,19,$$

$$\Delta_2 = 1,5 \cdot \frac{\sqrt{1+2\cdot 2\cdot (0,53)^2}-\sqrt{1+2\cdot 1\cdot (0,53)^2}}{2} = 0,16.$$

Analogous calculations have been performed for other sections.

The results of Δ_{1calc} and Δ_{2calc} calculations are summarized in Table 1. The Δ_{1emp} and Δ_{2emp} values obtained directly from the plots are also given in the table.

Table 1.

Z, cm	0	1	2	3	4	5	6	7
Δ_{1emp}	0,3	0,3	0,3	0,3	0,3	0,3	0,3	0,3
Δ_{1calc}	0,21	0,20	0,20	0,19	0,19	0,19	0,19	0,19
Δ_{2emp}	0,2	0,2	0,2	0,2	0,1	0,1	0,1	0,1
Δ_{2calc}	0,17	0,17	0,16	0,16	0,16	0,16	0,16	0,16

Apparently, the best agreement of empirical data with the calculated ones is observed for the first four plasmoid sections downstream. This fact can be explained by more precise approximation of the amplitude of the azimuth electric field in this area of a plasma bunch.

Procedures described in the present paper can be useful for a broad circle of experts in different fields of low-temperature induction plasma physics and engineering.

REFERENCES

[1] Gainullin R. N., Gerke A. R., Kirpichnikov A. P.// Izvestiya VUZov. Fizika. 1992. No. 6. p. 121.

[2] Gainullin R. N., Gerke A. R., Kirpichnikov A. P.// Inzh. Fiz. Zh. 1995. No. 2. p. 248.

[3] Gainullin R. N., Gerasimov A.V., Gerke A. R., Kirpichnikov A. P. Thermal and gasdynamic parameters of high-frequency induction plasma// Main directions of thermoelectric power development. Proceedings of the concluding scientific conference of teaching staff. Kazan branch of MPEI. Kazan, 1995, p. 91.

AN ITERATIVE DECODING AND ALGEBRA OF LOG-LIKELIHOOD FUNCTION

N.N.Tashatov

Eurasian National University named after L.N.Gumilev,
Astana, Republic of Kazakhstan, tash.nur@mail.ru

Abstract

Principles of the iterated turbo coding with combination of two or more composite codes have been considered in the article. Also fundamental statistical measures, such as a posterior probability and likelihood, which use for the description of the transfer reliability of the decoder with a soft entry and a soft exit, have been discussed.

1. INTRODUCTION

As a method of a high-performance code's obtaining the concatenated coding scheme by means of two or more composite codes combination has been offered by Forney [1]. Such codes can adjust errors in much longer codes, and they have structure which allows it to carry out decoding of average complexity rather easily. Sequential concatenated codes often use in systems with limitation of power, such as space sondes. The most widespread scheme contains an external Reed-Solomon code (the code is carried out first and removed last) which follows from an internal convolution code (it is carried out last and removed first) [2]. A turbo code is upgrade of the concatenated coding structure with iterated decoding algorithm of the linked code chain. A turbo coding is possible to present as a separate class in the reticulated sequences [3].

Turbo codes were first suggested in [4] by Berrou, Glavieux, Thitimajshima and then published in [5]. In the presented scheme the probability of emersion of errors attained 10^{-5} at coding extent equal 1/2 and BPSK modulations in the channel with additive white Gaussian noise (AWGN) with $E_b/N_0 = 0.7\,\text{dB}$. Codes are formed by combination of two or more composite codes which are different interleaving alternatives of the same informational sequence. In a case of convolution codes at a final stage the decoder gives out rigidly decoded bits or generally - the decoded symbols. In the turbo coding the decoding algorithm should not limit itself, submitting on decoders the rigid scheme of decisions. For the best use of the information received from each decoder, the decoding algorithm should apply, first of all, the soft scheme of decoding, instead of the rigid. For two-compound codes

systems the turbo decoding principle consists in transmitting the soft decision scheme from one decoder exit to an input of another and repeating this procedure until reliable decisions will be received.

2. PROBLEM DEFINITION

Likelihood functions. The applied systems, including AWGN channels, represent the greatest interest in communication. The most widespread form of a mathematical substantiation of hypotheses check criterion is the Bayes's Theorem, which expresses a posteriori probability (APP) solutions through a casual continuous variable x as [3]

$$P(d = i / x) = \frac{p(x / d = i)\, p(d = i)}{p(X)}, \quad i = 1, \ldots, M \tag{1}$$

and

$$p(x) = \sum_{i=1}^{M} p(x / d = i) P(d = i), \tag{2}$$

where

$P(d = i / x)$ is a posteriori probability;

$d = i$ presents data d, belonging to the class $\boldsymbol{i}$ of signals from a set M of classes;

$p(x/d = i)$ is a probability density function of an accepted analogue signal with noise x, at $d = i$; the parameter $p\ (d = i)$ is called as a priory probability and means probability of emersion of class i of signals.

Usually x represents observable casual variable or statistics underlying criterion, which is gained on an exit of the demodulator or any other processing device of signals. Therefore $p(x)$ is probabilities distribution function of the accepted signal x, giving test statistics in full space of signals classes. In the equation (1) at concrete observation the parameter $p(x)$ is scaling factor because it is gained by averaging on all classes of space. The small letter p is used for a designation of probabilities distribution function of a continuous casual variable and big letter P - for a probability designation (a priory and a posteriori). A posteriori probability definition of the accepted signal from the equation (1) is possible to represent as result of experiment. A priory probability $P\ (d = i)$ usually exists or is sized up before experiment. In experiment the equation (1) is used for calculation of a posteriori

probability, P ($d = i / x$). It is possible to consider it as "updating" of the available data gained at studying of the accepted signal x.

Example of the class from two signals. Let binary logical units 1 and 0 are represented by electric voltage +1 and -1. The variable d represents bit of the transmitted data (level of voltage or a logical unit). Let binary 0 (or electric voltage -1) will be a zero element at addition. The conditional function of probabilities distribution at a signal transmission on channel AWGN, presented as a likelihood function, is shown in a Figure 1.

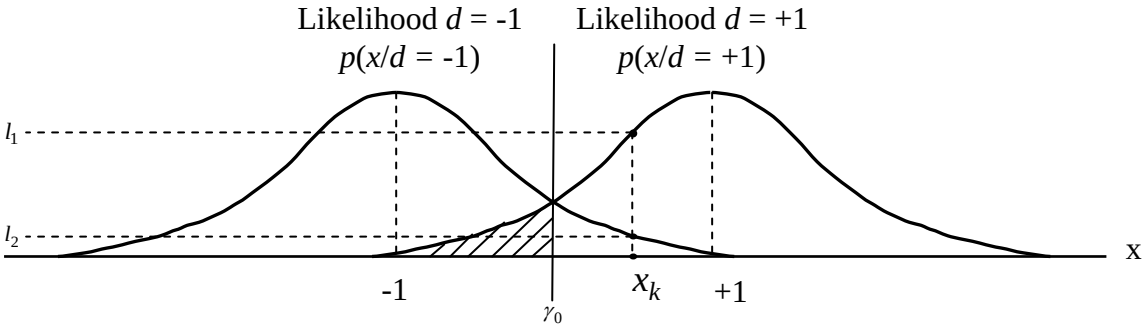

Figure 1 – Likelihood Function

Function p (x / i = +1), shown on the right, represents probabilities distribution function of a casual variable x which is transmitted provided that d = +1. Function, p (x / i = –1), shown at the left, represents the same function provided that d = –1. On an axis of abscissa the full range of possible values of test statistics x, forming in the receiver, is shown. In Figure 1 one value x_k is shown. Here index represents the observation which was made at value of time equal k. The perpendicular, lowered in a point x_k, intercrosses two curves of likelihood functions. As a result two values of a likelihood $l_1 = p\ (x_k / d_k = +1)$ and $l_2 = p\ (x_k / d_k = -1)$ are received. According to *a likelihood maximum principle*, the maximum value chosen from two available values l_1 or l_2. For each bit of data during the moment k we see that $d_k = +1$ if x_k gets on the right leg of a line of the decision-making designated γ_0, otherwise – $d_k = -1$.

The analogous rule of decision making known as *a maximum a posteriori probability* (MAP), can be presented as *a minimum probability of an error*, taking into consideration a priory probability of data. In general case rule can be expressed as follows:

hypothesis H_1 is chosen at $d = +1$, if a posterior probability

$$P\,(d = +1\,/\,x) > P\,(d = -1\,/\,x), \tag{3}$$

and hypothesis H_2 is chosen, at $d = -1$, if

$$P\,(d = +1\,/\,x) < P\,(d = -1\,/\,x). \tag{4}$$

Taking into account the equation (1), a posteriori probability can be substituted in the equations (3) and (4) by an equivalent expression. We shall receive the following equations:

hypothesis H_1 is chosen at $d = +1$, if

$$p(x/d=+1)P(d=+1) > p(x/d=-1)P(d=-1), \tag{5}$$

and if

$$p(x/d=+1)P(d=+1) < p(x/d=-1)P(d=-1), \tag{6}$$

then hypothesis H_2 is chosen, at $d = -1$.

Here the probability distribution function $p(x)$ from of both parts of an inequality has been excluded. The equations (5) and (6) define *a check of the likelihood functions ratio*, which can be written in following form:

hypothesis H_1 is chosen at $d = +1$, if

$$\frac{p(x/d=+1)}{p(x/d=-1)} > \frac{P(d=-1)}{P(d=+1)}, \tag{7}$$

and if

$$\frac{p(x/d=+1)}{p(x/d=-1)} < \frac{P(d=-1)}{P(d=+1)}, \tag{8}$$

then hypothesis H_2 is chosen, at $d = -1$.

These relations can be rewritten into

$$\frac{p(x/d=+1)P(d=+1)}{p(x/d=-1)P(d=-1)} > 1. \tag{9}$$

$$\frac{p(x/d=+1)P(d=+1)}{p(x/d=-1)P(d=-1)} < 1. \tag{10}$$

Log-likelihood ratio. Let apply taking the logarithm to a ratio of the likelihood functions which obtained in the equations (3) – (10). We will receive a metric convenient in many respects which is named as a log-likelihood ratio (LLR). This real representation of the soft solution out of decoder is defined by following expression

$$L(d/x) = \lg\left[\frac{P(d=+1/x)}{P(d=-1/x)}\right] = \lg\left[\frac{p(x/d=+1)P(d=+1)}{p(x/d=-1)P(d=-1)}\right] \tag{11}$$

so that

$$L(d/x) = \lg\left[\frac{p(x/d=+1)}{p(x/d=-1)}\right] + \lg\left[\frac{P(d=+1)}{P(d=-1)}\right] \quad (12)$$

or

$$L(d/x) = L(x/d) + L(d), \quad (13)$$

where L (x / d) is LLR of the test statistics x, obtained by measurements x on a channel exit at an interleaving of conditions that it can be transmitted d = +1 or d = –1, a L (d) – a priori LLR of the bit data d.

For denotations simplification we will rewrite the equation (13) as follows:

$$L'(\hat{d}) = L_c(x) + L(d). \quad (14)$$

here L_c (x) is obtained in a result of the channel measurements made in the receiver.

The equations (1) – (13) are received only from detector data. Further decoder introduction gives standard advantages of a decision scheme. For systematic codes it has been shown in [4], that LLR (the soft exit) out of the decoder is equal to the following:

$$L(\hat{d}) = L'(\hat{d}) + L_e(\hat{d}). \quad (15)$$

here $L'(\hat{d})$ is data bit's LLR out of the demodulator, i.e. on the decoder's entry, and $L_e(\hat{d})$ is named *external* LLR and represents the external information from the decoding process.

An output sequence of the systematic decoder is formed by data bits or parity bits. Taking into account the equation (14), equation (15) can be rewritten into

$$L(\hat{d}) = L_c(x) + L(d) + L_e(\hat{d}). \quad (16)$$

The equation (16) shows that output LLR of the systematic decoder consists of three components – channel measurement, a priori knowledge of data and external LLR of the decoder. In order to obtain $L(\hat{d})$, it is necessary to add separate contributions LLR, as shown in the equation (16) as all three components are statistically independent [4, 6]. The soft exit of decoder $L(\hat{d})$ is the real number providing adoption of the rigid solution and its reliability. Sign of the $L(\hat{d})$ sets the rigid solution: the solution will be equal d = +1 at positive sign $L(\hat{d})$, and d = –1 at the negative sign. Magnitude $L(\hat{d})$ defines reliability of this solution. Often

magnitude $L_e(\hat{d})$ owing to decoding has the same sign, as $L_c(x)+L(d)$ and consequently increases reliability of the $L(\hat{d})$.

3. RESULTS

Principles of iterated (turbo) decoding. In the typical receiver the demodulator often develops for solutions obtaining under the soft scheme and then the solutions will be transferred to the decoder. In AWGN channel increase of the transfer reliability in system, in comparison with a rigid decision scheme, is estimated approximately in 2 dB. Such decoder is the decoder with a soft entry and a rigid exit because final decoding process should be completed by bits (the rigid scheme). In the turbo codes two or several composite codes are used, and for iterations implementation the exit of one decoder is jointed to an entry of another, but the decoder with a rigid exit is undesirable. It is a consequence of that the rigid scheme in the decoder, in comparison with the soft scheme, reduces productivity of system. Therefore the decoder with a soft entry and a soft exit is necessary for implementation of the turbo decoding. Such decoder is shown in a Figure 2.

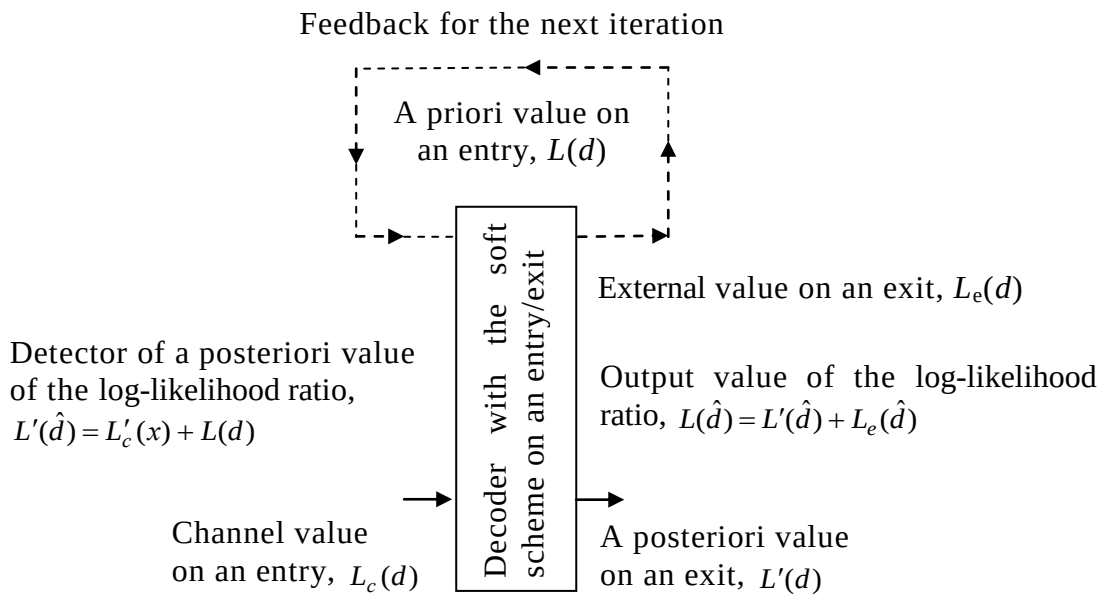

Figure 2 – Decoder with a soft entry and a soft exit

Let the data on such decoder during the first iteration are equiprobable. Then for the third member of the equation (12) initial a priori value LLR L (d) *will be equal* 0. If to take the log of the ratio of magnitudes l_1 and l_2 for defined values x (see a Figure 1) we will obtain channel value LLR L_c (x) which is the second member of the

equation (12). Exit of the decoder $L(d)$ in a Figure 2 is formed from LLR of the detector $L'(\hat{d})$ and external LLR of the exit $L_e(\hat{d})$ and show the data from decoding process. As is shown in a Figure 2 for iterated decoding, external likelihood is transferred back to an entry of other composite decoder for upgrade of a priory probability of the next iteration information.

Algebra of log of a likelihood function. To consider in detail the iterated feedback of the soft decoders exits, let's enter an algebra of log of a likelihood function [6].

Theorem: for statistically independent data d the sum of two log-likelihood ratios is defined as follows:

$$L(d_1) \boxplus L(d_2) \overset{def}{=} L(d_1) \oplus L(d_2) = \ln\left[\frac{e^{L(d_1)} + e^{L(d_2)}}{1 + e^{L(d_1)} e^{L(d_2)}}\right] \tag{17}$$

or

$$L(d_1) \boxplus L(d_2) \approx (-1) \times \operatorname{sgn}[L(d_1)] \times \operatorname{sgn}[L(d_2)] \times \min(|L(d_1)|, |L(d_2)|), \tag{18}$$

where sign «$\oplus$» means the sums modulo 2 of the data, which presented by binary digits;

sign $\boxplus$ uses for the sum denotation of logs of a likelihood functions or, the same, the mathematical operation presented by the equation (17). The sum of two LLR is defined as the sums modulo 2 basic statistically independent data bits.

The proof of the Theorem. Let's write log-likelihood ratio of a posterior probability of that the data bit is equal +1, to a posterior probability of that it is equal-1. As the hyperbolic logarithm basis is equale then log-likelihood ratio can be written as follows:

$$L(d) = \ln\left[\frac{P(d=+1)}{P(d=-1)}\right] = \ln\left[\frac{P(d=+1)}{1 - P(d=+1)}\right], \tag{19}$$

From here follows, that

$$e^{L(d)} = \left[\frac{P(d=+1)}{1 - P(d=+1)}\right]. \tag{20}$$

Let's find P (d = +1),

$$e^{L(d)} - e^{L(d)} \cdot P(d=+1) = P(d=+1), \tag{21}$$

$$e^{L(d)} = P(d=+1) \cdot \left(1 + e^{L(d)}\right), \tag{22}$$

$$P(d=+1)=\frac{e^{L(d)}}{1+e^{L(d)}}. \tag{23}$$

From the equation (23) follows, that

$$P(d=-1)=1-P(d=+1)=1-\frac{e^{L(d)}}{1+e^{L(d)}}=\frac{1}{1+e^{L(d)}}. \tag{24}$$

Let d_1 and d_2 are two statistically independent data bit, which set by voltage levels +1 and -1, corresponding to logic levels 1 and 0. Then addition d_1 and d_2 modulo 2 gives –1 if d_1 and d_2 have equal value, i.e. both are equal +1 or-1 simultaneously, and +1 if d_1 and d_2 have different values. Then

$$\begin{aligned} L(d_1 \oplus d_2) &= \ln\left[\frac{P(d_1 \oplus d_2=+1)}{P(d_1 \oplus d_2=-1)}\right]= \\ &= \ln\left[\frac{P(d_1=+1)\cdot P(d_2=-1)+\left[1-P(d_1=+1)\right]\cdot\left[1-P(d_2=-1)\right]}{P(d_1=+1)\cdot P(d_2=+1)+\left[1-P(d_1=+1)\right]\cdot\left[1-P(d_2=+1)\right]}\right]. \end{aligned} \tag{25}$$

Taking into account the equations (23) and (24), equation (25) can be rewritten into:

$$\begin{aligned} L(d_1 \oplus d_2) &==\ln\left[\frac{\left(\frac{e^{L(d_1)}}{1+e^{L(d_1)}}\right)\cdot\left(\frac{1}{1+e^{L(d_2)}}\right)+\left(\frac{1}{1+e^{L(d_1)}}\right)\cdot\left(\frac{e^{L(d_2)}}{1+e^{L(d_2)}}\right)}{\left(\frac{e^{L(d_1)}}{1+e^{L(d_1)}}\right)\cdot\left(\frac{e^{L(d_2)}}{1+e^{L(d_2)}}\right)+\left(\frac{1}{1+e^{L(d_1)}}\right)\cdot\left(\frac{1}{1+e^{L(d_2)}}\right)}\right]= \\ &= \ln\left[\frac{\left(\frac{e^{L(d_1)}+e^{L(d_2)}}{\left(1+e^{L(d_1)}\right)\cdot\left(1+e^{L(d_2)}\right)}\right)}{\left(\frac{1+e^{L(d_1)}e^{L(d_2)}}{\left(1+e^{L(d_1)}\right)\cdot\left(1+e^{L(d_2)}\right)}\right)}\right]=\ln\left[\frac{e^{L(d_1)}+e^{L(d_2)}}{1+e^{L(d_1)}e^{L(d_2)}}\right]. \end{aligned} \tag{26}$$

The equation (18) is an approximating of the equation (17). If one of LLR considerably exceeds second then an addition of LLR, defined by the equations (17) and (18), yields one very interesting result:

$L(d) \boxplus \infty = -L(d)$ и $L(d) \boxplus 0 = 0$

Here because of other sampling of a zero unit the algebra of log of a likelihood function differs from that which uses in [6] a little. In our case for a binary set (1, 0) by a zero unit it is chosen .

4. CONCLUSIONS

In the work the iterated turbo decoding principles are considered. The decision rule known as maxima a posterior probability is presented in the form of the minimum probability of an error. Also log-likelihood ratio and algebra of the probability function's logarithm are considered. The fundamental statistical measures, such as a posterior probability and likelihood, are used for the description of the transfer reliability of the decoder with a soft entry and a soft exit.

It has been shown, how the transfer reliability increases at turning on of the cascade decoder with a soft exit in decoding iterative process. Mathematics of the decoder, which based on a principle of the maximum a posteriori, has been discussed.

REFERENCES

[1] Forney G.D.Jr. Concatenated Codes. Cambridge, Massachusetts: M. I. T. Press, 1966.

[2] J.H. Yuen, et. al. Modulation and Coding for Satellite and Space Communications. Proc. IEEE, vol. 78., n. 7, July, 1990, pp. 1250 – 1265.

[3] Sklyar B. Digital communication. Theoretical bases and practical application. Moscow: Williams, 2004.

[4] Berrou C., Glavieux A. and Thitimajshima P. Near Shannon Limit Error – Correcting Coding and Decoding: Turbo Codes. IEEE Proceedings of the Int. Conf. on Communications, Geneva, Switzerland, May, 1993 (ICC'93), pp. 1064 – 1070.

[5] Berrou C., Glavieux A. Near Optimun Error Correcting Coding and Decoding: Turbo – Codes. IEEE Trans. on Communications, vol. 44, n. 10, October, 1996, pp. 1261 – 1271.

[6] Hagenauer J. Iterative Decoding of Binary Block and Convolutional Codes. IEEE Trans. On Information Theory, vol. 42, n. 2, March, 1996, pp. 429 – 445.

AN EOG BASED HUMAN COMPUTER INTERFACE SYSTEM FOR ONLINE CONTROL

(Selected from CEMA'10 Conference)

Carlos A. Vinhais, Fábio A. Santos and Joaquim F. Oliveira

Departamento de Física, Instituto Superior de Engenharia do Porto
Rua Dr. António Bernardino de Almeida, 431, 4200-072 Porto, Portugal
cav@isep.ipp.pt

Abstract

Human to machine interfaces have received more and more attention of researchers in recent years. Electrooculography (EOG) is a new technology to sense eye signals and can be used as an efficient bio-based human computer interface (HCI). The paper is concerned with the design and implementation of an eye movement detection system for biomedical research. The described system includes several electronic units for acquisition, conditioning, amplification and noise filtering of measured voltage signals. Analog to digital conversion of such biopotentials is achieved with an Arduino BT board. With its built-in Bluetooth module, it allows for wireless communication to personal computers for further signal processing and analysis. Experimental results based on real-life EOG signals show that the developed system is efficient in terms of accuracy and applicability. The proposed solution is a low-cost general purpose EOG-based HCI system that can be used by patients with disabilities for communication.

1. INTRODUCTION

Traditional methods of control or communication between humans and machines, e.g. mouse and keyboard, require a certain control motor on the part of the users. However, many people with severe disabilities only retain their control capacity over the oculomotor system. Therefore, the focus on the development of new human computer interface (HCI) and communication systems based on the detection of eye position has increased in the last years.

Electrooculography (EOG) is a new technology of recording both horizontal and vertical eye movements, by measuring, in real time, very small electrical potentials that exist across the cornea and the retina. Such signals are easily detected by placing electrodes on user's forehead around the eyes. Also, the relationship between EOG waveforms and eye movements is almost linear.

EOG based HCI is becoming the hotspot of bio-based HCI research in recent years, since it provides users with a degree of independence in the environment. This method was used as the guidance strategy in assistive devices for controlling wheelchairs for disabled people [1]. It also represents an efficient computer interface to improve communication abilities of those patients [2,3,6]. EOG has also been used as a measurement device used in psychophysiological tests as research equipment for recording facial expressions during human emotion studies [4]. Furthermore, applications can be extended to normal persons as well, in robotics and entertainment.

As a contribution in this area of biomedical research, we present a general purpose EOG based HCI system for online control. The proposed approach includes several electronic modules for acquiring and filtering EOG waveforms, generated from different eye movements such as looking up/down, right/left and eye blinking. The system also provides wireless data transmission to a personal computer (PC) for further signal processing and analysis.

The paper is organized as follows: Section 2 introduces the fundamental principles of detecting and acquiring EOG signals. Section 3 describes the design of the proposed HCI system in detail. Experimental results of several eye movements and blinking are illustrated in Section 4 and the conclusion is given in Section 5.

2. EOG DETECTION PRINCIPLES

EOG is a method for sensing eye movement and is based on recording the standing corneal-retinal potential arising from hyperpolarizations and depolarizations existing between the cornea and the retina [1]. Such biopotential, commonly known as an electrooculogram, is captured by five surface electrodes placed around the eyes, as shown in Figure 1.

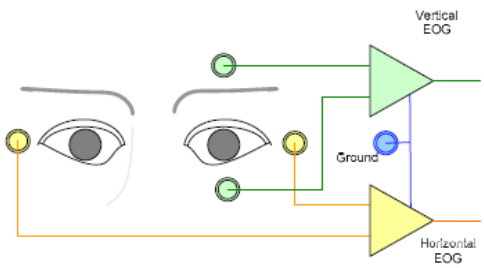

Figure 1. Electrodes placement [2,5].

Independent measurements can be obtained: two electrodes are placed on the temples to detect horizontal movements, while another pair above and below the eye is used to detect vertical motion and eye blinking. A reference electrode (ground) is placed on the forehead or at the mastoid [6].

The corneal-retinal potential is roughly aligned with the optic axis and hence rotates with the direction of gaze. When the gaze is shifted, positive or negative pulses will be generated when the eyes are rolling, e.g. upward or downward. The amplitude of EOG pulses will be increased with the increment of rolling angle, and their width is proportional to the duration of the eyeball rolling process.

EOG values vary from tens to hundreds of μV, with a frequency range of about DC-100 Hz. The EOG signal changes approximately 20 μV for each degree of eye movement and is practically linear for gaze angles up to 30º [1]. Therefore, with proper calibration, EOG can be used to accurately specify the angular position of the eyeball in both vertical and horizontal channels.

3. HCI SYSTEM DESIGN

The block diagram of the proposed HCI system is shown in Figure 2. The system is microcontroller (μC) based, battery powered, and is composed of four main parts or units: signal pre-amplification, signal filtering, analog to digital conversion (ADC) and data transmission to PC.

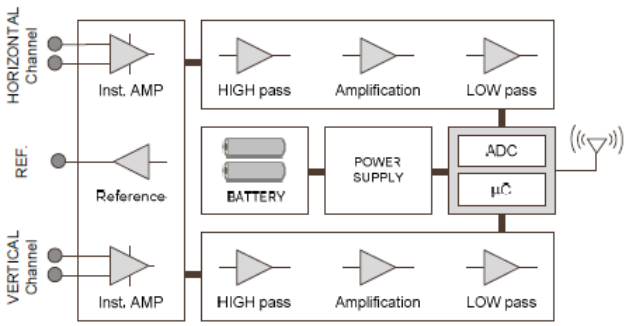

Figure 2. EOG based HCI system block diagram.

Five Ag/AgCl electrodes (two for each channel and one for ground) are used to acquire EOG signals. The pre-amplification circuit is intended to amplify the signals to appropriate amplitude. The EOG signal filtering unit includes a band-pass analog

filter (a combination of high-pass and low-pass filter) to remove the baseline and higher frequency interference. The total gain of the system is achieved by implementing signal amplification into two stages, each having a fixed gain. Analog to digital conversion is then performed, and horizontal and vertical EOG signals are finally transmitted to the PC serial port over Bluetooth wireless technology. Free open source is used to program the microcontroller and display EOG waveforms in real-time.

3. 1. Power Supply

The whole circuit is operated from a single +5 V power supply, by using a 7805 voltage regulator. The chip ICL7660 was used to perform supply voltage conversion, resulting in complementary output voltage –5 V. The circuit has been powered with a simple +9 V battery.

3. 2. Pre-amplification

According to the characteristics of EOG signals, the differential amplifier chip INA126P was selected for the acquisition and pre-amplification step, as it can handle EOG signals in μV range. The INA126P is a precision instrumentation amplifier for accurate, low noise differential signal acquisition. The gain of the INA126P is set by simply adjusting the value of a single external resistor R_G:

$$G_1 = 5 + \left(80\ \text{k}\Omega / R_G\right) \tag{1}$$

A protection system in the form of an RC low-pass filter was also implemented at the INA126P's inputs, in order to remove electro-static discharge and radio frequency interference [2].

3. 3. Reference Electrode

To improve the INA126P's common mode rejection ratio (~94 dB), a driven-right leg circuit was implemented. Here, a low-noise high-precision OPA2227 dual amplifier was used. This circuit reads what it believes to be noise and transfers a minute signal back to the body through reference electrode to negate its effect. This technique is normally used in medical operations when reading a very small electrical potential from the body.

3. 4. Signal Filtering

A critical issue in accurately acquiring and amplifying the EOG potential, is overcoming a substantial DC offset generated by the potential difference between the reference electrode and each of the active electrodes. For reducing DC offset and some other shifting resting potentials, an active high-pass filter is employed with cutoff frequency at 0.20 Hz. Once DC component is removed, an OPA227 amplifier circuit is designed to complement the entire magnification required. The formula for gain depends on two resistors R_A and R_B:

$$G_2 = 1 + \left(R_B / R_A\right) \tag{2}$$

The power line noise and high frequency components of EOG signals are then greatly reduced with low-pass filtering. A cutoff at 32 Hz was selected due to bandwidth of EOG signals. A single OPA4227 was used to implement both 4th order Bessel filters.

3. 5. Data Acquisition

After all amplifications and filtrations, EOG signals are digitized and transferred to PC. Analog to digital conversion with 10 bits of resolution is done using a microcontroller board *Arduino* BT [7]. Since it supports wireless serial communication over Bluetooth, software was written in *Processing* [8] to read incoming data from the PC serial port and display the measured signals on the screen saved real-time.

4. EXPERIMENTAL RESULTS

In building the whole circuit, number of components was tried and final component selection was based on optimal performance. Therefore, the two-stage signal amplification was implemented by using R_G = 806 Ω, R_A = 994 Ω and R_B = 55.8 kΩ. From equations 1 and 2, G_1 = 104 and G_2 = 57. Thus, for each EOG channel, the total gain of the system was set to $G = G_1 * G_2 = 5928$. Some examples of EOG waveforms acquired from horizontal and vertical eye movements and eye blinking are shown in Figure 3.

All signals were sampled at 100 Hz (10 ms per sample), which rightly follows the Nyquist rate. Experiments with higher sampling frequency (500 Hz and 1 kHz) were also performed. In all cases, similar results were obtained.

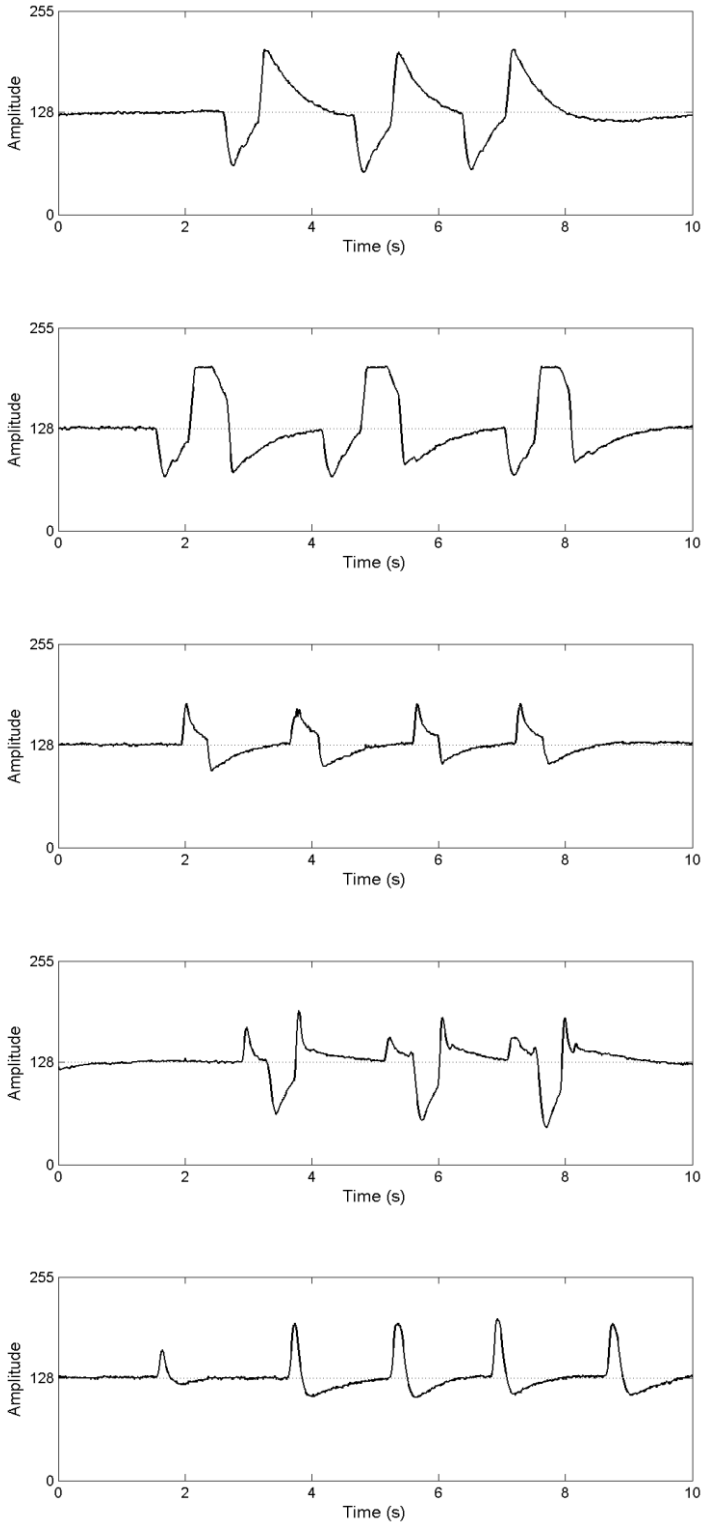

Figure 3. EOG waveforms. From top to bottom: Center–RIGHT, Center–RIGHT–LEFT, Center–UP, Center–UP–DOWN and eye blinking.

5. CONCLUSION

A general purpose EOG based HCI system for eye movement detection was presented. With a simple design, the system is μC-based, battery powered and supports wireless data transmission to PC. The results show that the proposed system has stable performance and can be used as an effective low-cost solution for online control applications.

REFERENCES

[1] R. Barea, L. Boquete, M. Mazo, and E. López, System for Assisted Mobility Using Eye Movements Based on Electrooculography, *IEEE Trans. on Neural Systems and Rehabilitation Engineering*, 10(4), 209-218 (2002).

[2] A. Q. Malik, and J. Ahmad, Retina Based Mouse Control (RBMC), *World Academy of Science, Engineering and Technology*, 31, 318-322 (2007).

[3] A. B. Usakli, S. Gurkan, F. Aloise, G. Vecchiato and F. Babiloni, On the Use of Electrooculogram for Efficient Human Computer Interfaces, *Computational Intelligence and Neuroscience*, Vol. 2010, Article ID 135629, 5 pages (2010).

[4] A.T. Vehkaoja *et al.*, Wireless Head Cap for EOG and Facial EMG Measurements, *Conf Proc. IEEE Eng Med Biol Soc*, 5865-5868 (2005).

[5] Y. Chen, "Design and evaluation of a human-computer interface based on electrooculography", *Master Thesis* (2003) *unpublished*.

[6] Zhao Lv, Xiao-Pei Wu, Mi Li and De-Xiang Zhang, Development of a human computer Interface system using EOG, *Health*, 1, 39-46 (2009).

[7] *Arduino* – http://arduino.cc/

[8] *Processing* – http://processing.org/

FDTD MODELING OF REFRACTOMETRIC OPTICAL SENSORS BASED ON QUASI-ONE-DIMENSIONAL PHOTONIC CRYSTALS

(Selected from CEMA'10 Conference)

G. S. Kliros* and K. A. Papageorgiou

Hellenic Air-Force Academy, Department of Aeronautical Sciences
Division of Electronics and Communication Engineering
Dekelia Air-Force Base, Attica GR-1010, Greece
*e-mail: gsksma@hol.gr

Abstract

We report on the design of a refractometric optical sensor based on a quasi-one dimensional photonic crystal structure etched in a Si_3N_4 ridge waveguide grown on top of a SiO_2 substrate. A photonic crystal based on this kind of structure exhibits a photonic bandgap for TE polarized light. The finite difference time domain method (FDTD) is employed in order to design the device and investigate its transmission spectra and sensitivity characteristics. The shift in the central wavelength of the reflectivity spectrum, due to change in the refractive index, when the low-index areas of the photonic crystal are infiltrated with different fluids, is found to be linear and hence, suitable for refractrometric sensing applications.

1. INTRODUCTION

Integrated optical sensors have a high potential to be employed as devices in many areas such as, microbiology, environmental safety, defence and aerospace technology. Their main advantages are immunity to electromagnetic interference, high compactness and robustness and prospects of mass production, and also they have fast responsivity and higher sensitivities when compared to Micro-Electro-Mechanical Systems (MEMS). In a variety of environmental, biomedical and aerospace applications, the measurement of the refractive index is very important since is strongly related to structure composition.

Photonic crystals (PC) and photonic band gap structures (PBG) [1] are very promising building blocks for photonic components of submicron scale which is comparable to that of their electronic counterparts. Two-dimensional (2D) PCs formed in a dielectric slab waveguide structure have attracted much interest recently for realizing novel micro-optoelectronic devices [2-5]. A structure having a periodic index modulation in one dimension is known as a one-dimensional photonic crystal (1D-PC). If the structure has non-periodic features in the other two dimensions, it is

denoted as a quasi-1D PC which is essentially a 'Bragg grating'. A Bragg grating with a strong index modulation shows a typical property of PCs: an extended transmission stop-band. The width of this stop-band and the steepness of its edges increase with the strength of the refractive index modulation. For sensing applications, one has to exploit the steep edges of the stop-band in a strong grating [6].

In this paper, motivated by the recent interest in developing quasi-1D PC sensors [7,8], we designed and simulated a wide ridge-type channel waveguide of silicon nitride with a 1D PC etched into the core layer. The reflectivity spectrum of the device has been obtained using the FDTD method. The sensitivity of our device is determined by observing the shift in the central wavelength of reflectivity spectrum as a function of the change in effective refractive index.

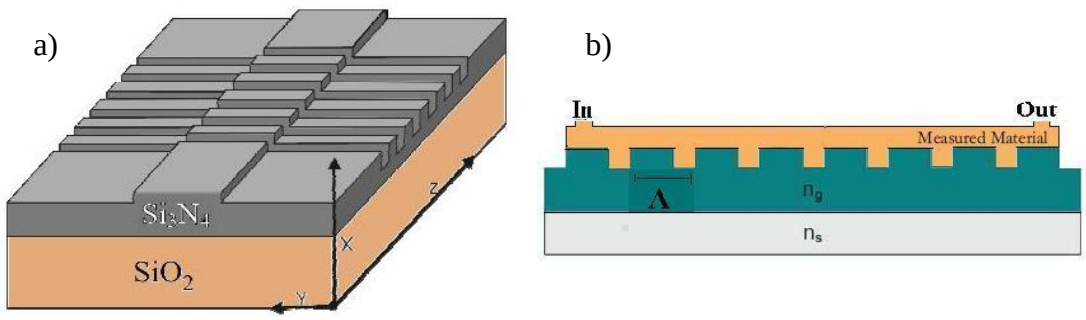

Figure1. Schematic 3D drawing of the waveguide with a 1D photonic crystal (a) and Cross-section of the quasi one-dimensional photonic crystal sensor with a cuvette placed on top (b).

2. DEVICE DESIGN AND MODELING

A schematics of the 3D-structure as well as the cross-section of the device is shown in Fig.1. The sensing element is a strong grating in a Si_3N_4 ridge waveguide (n_g=2.01) with period Λ=628.2 nm grown on top of a SiO_2 substrate (n_s=1.46) resulting in TE single-mode operation at wavelengths around the modern telecommunications wavelength of λ=1.55 μm. The light is guided by the photonic crystal structure in the horizontal plane and is confined by the classical ridge waveguide in the vertical direction. The sensitivity of the sensor for changes in the refractive index can be simulated by infiltrating the grooves of the grating with different fluids through the cuvette, as it is shown schematically in Fig. 1(b).

The simulation is performed using the Finite Difference Time Domain Method (FDTD) with Perfectly Matched Layer (PML) boundary conditions. Since the waveguide thickness is very small and there is no structural variation in the y-direction uniformly over the x-z plane, the structure can be analyzed as a quasi-1D

device without losing much generality. FDTD method relies on the discretization of Maxwell's equations and provides the description of the time evolution of the electromagnetic field without any assumption about the number and the characteristics of the propagating modes.

According to FDTD method on a Yee cell [9], the following simple set of discrete field equations is obtained:

$$E_x^{n+1}(i) = E_x^n(i) + \frac{\Delta t}{\varepsilon(i)\Delta z}\left[H_y^{n+\frac{1}{2}}(i+1/2) - H_y^{n+\frac{1}{2}}(i-1/2)\right] \quad (1)$$

$$H_y^{n+\frac{1}{2}}(i+1/2) = H_y^{n-\frac{1}{2}}(i+1/2) + \frac{\Delta t}{\mu(i)\Delta z}\left[E_x^n(i+1) - E_x^n(i)\right] \quad (2)$$

where Δt and Δx are the finite difference cells in the temporal and spatial domain, respectively. A 1D-mesh grid with size of Δx=12.035 nm is used in the simulation. The time step is based on the Courant's condition $\Delta t = \Delta x / \sqrt{2}c$, where c is the velocity of light in vacuum. The simulation is run for 131.072 (2^{17}) time steps to get a fine spectral resolution. Vector-based computations are employed instead of element-based ones using MATLAB technical language in order to reduce the computation time considerably. The source employed was a Gaussian modulated continuous wave at the central wavelength of 1.55 μm having a broad spectral bandwidth. By Fast-Fourier-Transforming (FFT) the electric field component, sampled at the output, the frequency response of the device under investigation was obtained, with just a single simulation run.

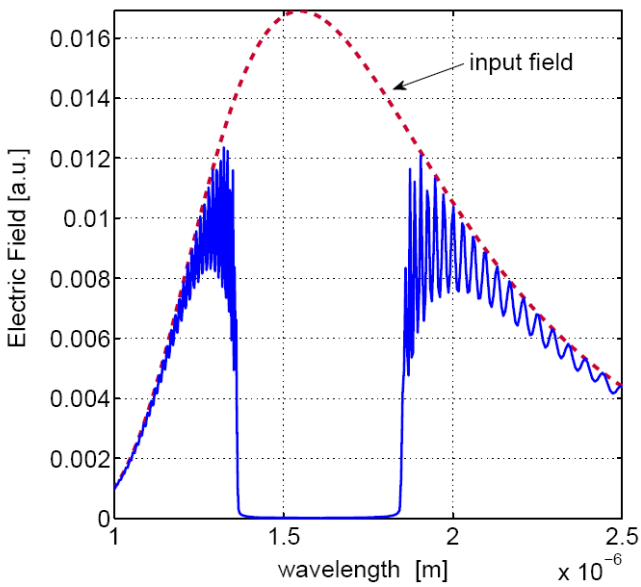

Figure 2. Spectral dependence of the electric field intensity when the grooves are filled with air. The dashed line represents the spectral dependence of the input pulse.

In order to get an exact Bragg wavelength from the FDTD simulation, the effective index corresponding to TE-mode propagating in the ridge waveguide, is set to a value n_{eff}=1.61 which is obtained from a Beam Propagation Method (BPM) mode solver [10]. For first-order gratings like in Fig. 1(b), the Bragg conditions are expressed as

$$\Lambda_{tooth} = \frac{\lambda_{Bragg}}{4n_{eff,tooth}}, \quad \Lambda_{groove} = \frac{\lambda_{Bragg}}{4n_{eff,groove}} \tag{3}$$

For the desired Bragg wavelength of 1.55 μm, Λ_{tooth}=240.7nm and Λ_{groove}=387.5 nm so that a grating period Λ= 628.2 nm, is obtained. The number of periods chosen was 64, resulting in an overall grating length of 40.2 μm.

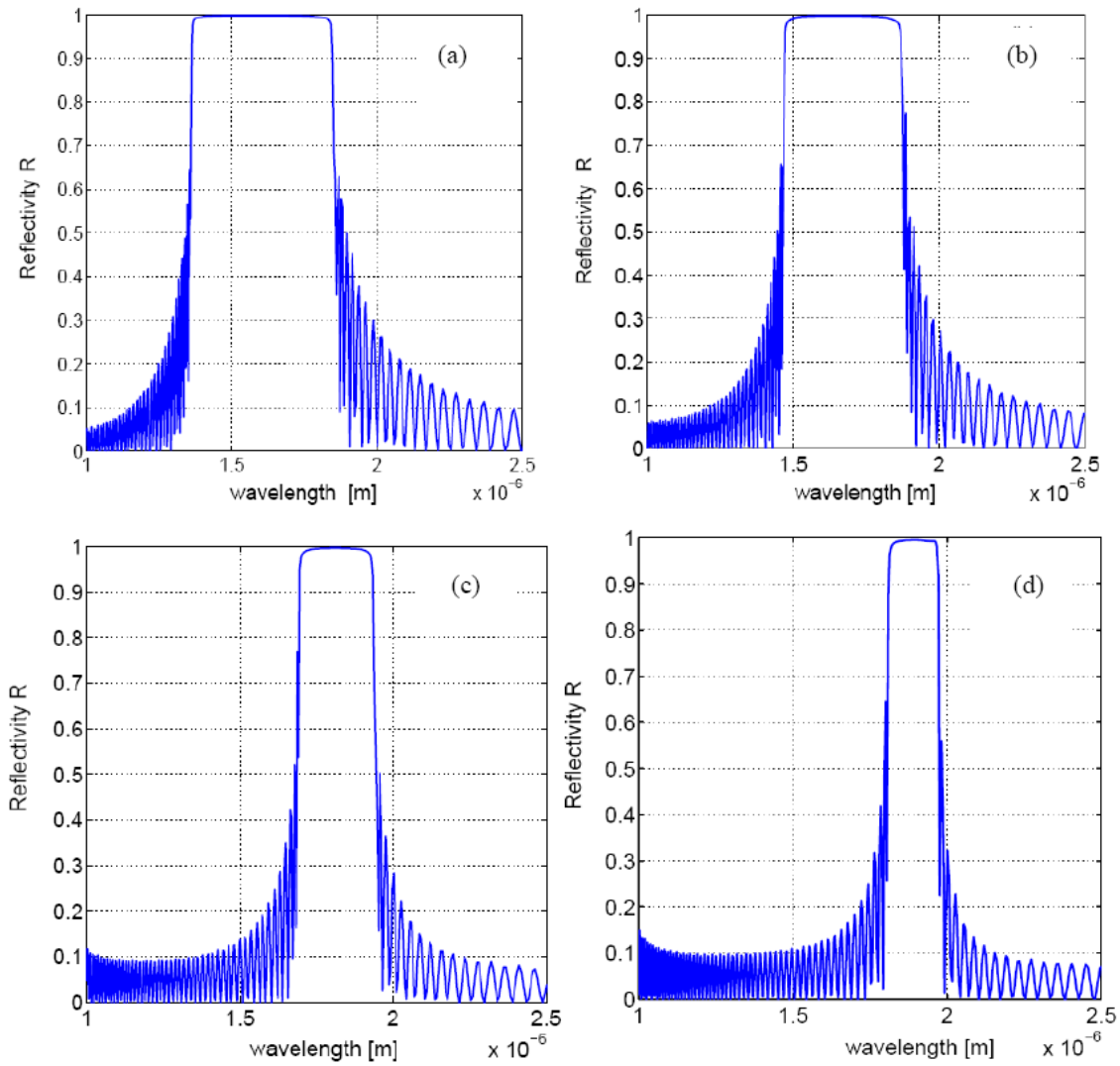

Figure 3. Computed reflectivity spectra when the refractive index of infiltrated grating grooves is (a) n_c=1.0 (b) n_c=1.1, (c) n_c=1.3 and (d) n_c=1.4

3. RESULTS AND DISCUSSION

Figure 2 shows the spectral intensity of both the input and the transmitted electric field for air-filled grooves. The wide stop band in the transmission spectrum would allow a high free spectral range, so that the Bragg wavelength can be tuned over a wide range of wavelengths. Table I reports the shift of the central wavelength when the grating grooves are infiltrated by different fluids with increasing refractive indices. Experimentally, a continuous change in refractive index could be realized by mixing together two fluids with different indices. As it is seen, the central wavelength i.e. the wavelength exactly in the middle of the stop-band defined by the -3 dB point of the stop-band edges, is shifted towards higher wavelength values as a consequence of the change of the guided mode effective index.

Figures 3(a)-3(d) illustrate the effect of fluid refractive index change on the reflectivity of the quasi-1D photonic crystal structure. Both edges of the stop-band are shifted toward longer wavelengths. A small wavelength shift of such an edge can cause a large change in the transmitted power from a source having an appropriate wavelength.

Grating sensitivity describes the device efficiency when it works as a sensor. In this work, we define the sensitivity as

$$S = \frac{\partial \lambda_{centre}}{\partial n_c} \tag{4}$$

and therefore, it can be easily calculated using the data of Table I.

Table I: Resonance central wavelength for different refractive indices.

n_c	λ_{low} (nm)	λ_{high} (nm)	λ_{centre} (nm)
1.00	1356.7	1857.8	1607.2
1.05	1409.6	1874.8	1642.2
1.10	1466.4	1881.4	1673.9
1.15	1520.2	1896.0	1708.1
1.20	1576.0	1912.0	1744.0
1.25	1631.5	1929.7	1780.6
1.30	1687.3	1944.4	1815.9
1.35	1749.5	1956.4	1852.9
1.40	1806.5	1974.8	1890.7
1.45	1863.2	1993.9	1928.5
1.50	1921.0	2013.5	1967.3

Fig. 4 presents the central wavelength shift ($\Delta\lambda_{centre}$) as a function of the change in fluid refractive index by infiltration of the grating grooves, where the reference wavelength is the central wavelength for air-filled grooves. From the graph, it is observed a 7 nm shift of the centre wavelength for a change in refractive index δn_c=0.1 and therefore an average sensitivity S~70 nm per unit refractive index change is obtained. Furthermore, the central wavelength shift is linear and hence, the device is extremely suitable for sensing applications.

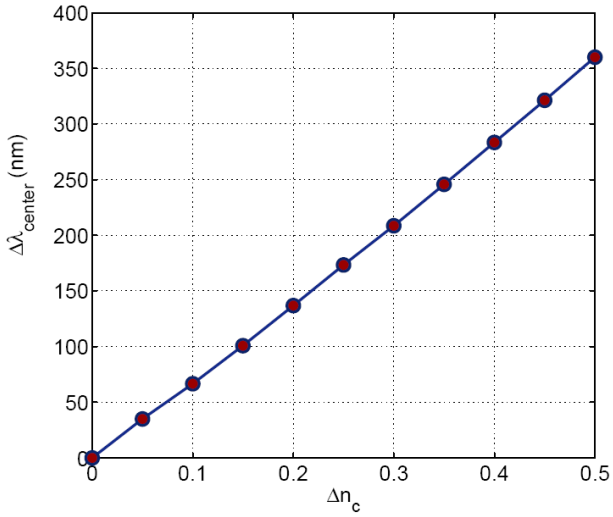

Figure 4. Sensitivity characteristic curve showing the simulated changes in central wavelength versus changes in refractive index.

4. CONCLUSION

We have designed and simulated a very compact refractometric sensor based on quasi-1D photonic crystal. The FDTD simulation method is employed, in order to investigate its transmission spectra and sensitivity characteristics. For the working wavelength of ~1.55 μm, the transmission spectrum has been calculated by changing the refractive index of different fluids in the grooves of the grating. It is found that, increasing the refractive index, the wavelength position of both the lower and upper band edge are shifted with the largest shift appeared in the lower wavelength band edge. The shift in the central wavelength is found to be approximately linear and hence, the device is extremely suitable for sensing applications. The simulated structure shows good performance in terms of compactness, sensitivity and free spectral range. The performance of the designed device as temperature, pressure or strain sensor based on the thermo-elastic and thermo-optic effects [11] will be reported in a future paper.

REFERENCES

[1] P. Markos and C. M. Soukoulis, *Wave Propagation: From Electrons to Photonic Crystals and Left-handed Materials*, Princeton University Press, New Jersey, 2008.

[2] R. V. Nair and R. Vijaya, "Photonic crystal sensors: An overview", *Progress in Quantum Electronics*, vol. 34, 2010, pp. 89-134.

[3] G. S. Kliros, A. N. Fotiadis and G. P. Tziopis, "Optical Simulation of Silicon-Based Complete Photonic Bandgap Modulator", *Proc. of 21thIEEE Int. Conference on Microelectronics*, Marrakesh**,** Morocco, 2009, pp. 219-221.

[4] G. S. Kliros, A. N. Fotiadis and G. P. Tziopis, "Design of silicon optical modulator based on complete TM photonic band-gap", *Optoelectronics and Adv. Mat.-Rapid Communications',* vol. 3, No. 7, 2009, pp. 655 – 658.

[5] G. S. Kliros and K. A. Papageorgiou, "Refractometric Optical Sensor based on Tapered Photonic Crystal Waveguide", *J. Optoelectronics Adv. Mater.*, vol.12 (7), 2010, pp. 1530-1533.

[6] W. C. L. Hopman *et. al.*, "Quasi-1D Photonic Crystal as a Compact Building-Block for Refractometric Optical Sensors", *IEEE J. Sel. Top. Quant. Electron.* vol. 11, 2005, pp. 11-16.

[7] V. M. N. Passaro *et. al.*, "Design of Bragg Grating Sensors Based on Sub-micrometer Optical Rib Waveguides in SOI", *IEEE Sensors J.* vol. 8, 2008, pp.1603-1611.

[8] A. Banerjee, "Binary number sequence multilayer structure based on refractometric optical sensing element", *J. Electromagn. Waves and Appl.*, vol. 22, 2008, pp. 2439 -2449.

[9] A. Taflove, *Computational Electrodynamics: The Finite-Difference Time-Domain Method*, 2nd edn., Artech House, 2000.

[10] Em. E. Kriezis *et. al.*, "Full vector beam propagation method for axially dependent 3-D structures", *IEEE Trans. Magnetics*, vol. 33 (2), 1997, pp. 1540-1543.

[11] H. M. Chong and R. De La Rue, "Tuning of photonic crystal waveguide microcavity by thermo-optic effect", *IEEE Photon. Techn. Lett.***,** vol. 16 (6), 2004, pp. 1528-1530.